Journal of Materials Science & Technology 236 (2025) 1–18

Contents lists available at ScienceDirect

Journal of Materials Science & Technology

journal homepage: www.elsevier.com/locate/jmst

Research Article

Enhanced mechanical and electrical properties of Cu-Ni-Be alloys through rotary swaging and aging treatment

Kaixuan Zhou[a,1], Yonghao Zhao[a,b,1,*], Qingzhong Mao[a], Shunqiang Li[a], Jizi Liu[a,c,*]

[a] Nano and Heterogeneous Materials Center, Nanjing University of Science and Technology, Nanjing 210094, China
[b] School of Materials Science and Engineering, Hohai University, Changzhou 213200, China
[c] Nanjing Research Center for Biomedical Electron Microscopy (NRC-BEM), Medical School, Nanjing University, Nanjing 210093, China

ARTICLE INFO

Article history:
Received 14 December 2024
Revised 19 January 2025
Accepted 23 January 2025
Available online 3 April 2025

Keywords:
Cu-Ni-Be alloy
Rotary swaging
Comprehensive performance
Industrial applications

ABSTRACT

High-performance copper alloys with enhanced strength, conductivity, and toughness are critical in industrial applications, yet achieving this combination of properties in a bulk form remains challenging, as many strength-enhancing grain refinement methods are limited to small-scale production. This study investigates the development of Cu-Ni-Be alloys with high strength, high conductivity, and excellent ductility using rotary swaging (RS) as the primary processing method, followed by aging treatments. The RS process, known for its advantages in industrial-scale applications, enables the formation of fibrous, elongated grains with strong axial alignment, resulting in improved conductivity along the wire direction. Additionally, the triaxial compressive stresses inherent in RS promote effective dislocation accumulation, producing an alloy with a strength of 706 MPa, uniform elongation of 1.4 %, and conductivity of 35 % international annealed copper standard (IACS) in the as-swaged state. Optimized aging treatments further improve the comprehensive performance of the alloy, increasing its strength to 1064 MPa, uniform elongation to 10.4 %, and conductivity to 46 % IACS through the formation of dispersed nanoscale precipitates. These findings demonstrate that the Cu-Ni-Be alloy processed by RS and aging achieves a unique balance of tensile strength, ductility, and conductivity, making it highly suitable for industrial applications. This establishes RS as a viable approach for producing advanced Cu-Ni-Be alloys with tailored properties for the electrical and structural industries.

1. Introduction

High-strength, high-conductivity, and high-ductility copper alloys are essential materials in various industrial applications, including electrical power systems, aerospace, and automotive industries [1,2]. These alloys offer a unique combination of mechanical strength and electrical conductivity, making them ideal for components that require efficient electrical performance without compromising structural integrity [3]. Traditional copper alloys often face a trade-off between strength and conductivity; enhancing one property typically leads to the detriment of the other. Therefore, developing copper alloys that simultaneously achieve high strength, high conductivity, and excellent ductility remains a significant challenge in materials science.

Copper-beryllium (Cu-Be) alloys have been widely studied due to their remarkable mechanical properties and good electrical conductivity [4,5]. The addition of nickel (Ni) to Cu-Be alloys further enhances their strength through solid-solution strengthening and precipitation hardening mechanisms. Precipitation of metastable phases such as γ'' and γ' during aging treatments contributes to increased hardness and strength while maintaining acceptable levels of electrical conductivity [6].

However, the traditional two-step processing method of solution treatment followed by aging (Route A) typically results in Cu-Ni-Be alloys with a yield strength not exceeding 600 MPa [7]. This is due to the coarse grain microstructure induced by solution treatment at temperatures above 800 °C, which limits the contribution of grain boundary (GB) strengthening to the material's overall strength. The relatively low strength of the material can be improved by incorporating plastic deformation into the processing route [8]. However, plastic deformation significantly reduces the ductility and electrical conductivity of metals and alloys, as the increased dislocation and GB densities result in a loss of work hardening ability [9] and enhanced electron scattering [10]. For instance, after undergoing solution treatment, equal channel angular pressing, and aging (Route B), the CuCoNiBe alloy exhibits refined

---

[*] Corresponding authors.
E-mail addresses: yhzhao@njust.edu.cn (Y. Zhao), jzliu@njust.edu.cn (J. Liu).
[1] These authors contributed equally to this work

https://doi.org/10.1016/j.jmst.2025.01.073
1005-0302/© 2025 Published by Elsevier Ltd on behalf of The editorial office of Journal of Materials Science & Technology.

Table 1
Chemical composition of Cu-Ni-Be alloy (wt.%).

Ni	Be	Al	Fe	Si	Total others	Cu
1.606	0.508	0.007	0.022	0.009	< 0.038	Bal.
1.4–2.2	0.2–0.6	< 0.2	< 0.1	< 0.2	–	–

equiaxed grains and a high density of low-angle grain boundaries (LAGBs), resulting in a 270 MPa increase in yield strength compared to the coarse-grained material processed via Route A. However, its uniform elongation and electrical conductivity are only 32 % and 82 % of those achieved by Route A, respectively [8]. Therefore, it is crucial to select appropriate plastic deformation methods to strengthen the material while minimizing reductions in ductility and electrical conductivity, thereby enhancing the overall performance of the material and facilitating its industrial applications.

Directional design in materials processing has emerged as a promising approach to tailor the microstructure and properties of metallic alloys. By inducing specific textures and grain orientations, it is possible to optimize the balance between strength and conductivity [11,12]. Rotary swaging (RS) offers several advantages over traditional deformation processes. One of the key benefits is the ability to produce infinitely long products with consistent cross-sectional dimensions, making it suitable for industrial-scale manufacturing [13]. The triaxial compressive stresses involved in RS facilitate the effective accumulation of dislocations [14], leading to significant strain hardening and grain refinement without introducing excessive tensile stresses that could cause cracking. Thus, bulk high-strength nanocrystalline (NC) Mg-Gd-Y-Zr and AZ31 alloys [15–17], Cu and Cu-Cr [11–13], Al and Al matrix composites [18–20] as well as commercial-purity Ti [21], etc. can be successfully prepared by using RS [22,23]. Additionally, the process promotes the development of fibrous microstructures, which are beneficial for both mechanical strength and electrical conductivity along the deformation direction [24].

In this study, we explore the use of RS combined with subsequent aging treatments to process Cu-Ni-Be alloys. The goal is to develop a material with a superior combination of high strength, high ductility, and high electrical conductivity suitable for industrial applications. By leveraging the advantages of RS and the precipitation-hardening potential of Cu-Ni-Be alloys, we aim to overcome the traditional trade-offs between mechanical and electrical properties in copper-based materials. The effects of deformation and aging on the microstructural evolution, texture development, and resulting properties are systematically investigated to provide insights into the mechanisms contributing to the enhanced performance of the alloy.

2. Materials and methods

2.1. Material preparation process

The commercial Cu-Ni-Be alloy grade C17510, with the specific chemical composition detailed in Table 1, was analyzed using a direct-reading spectrometer (Spectro M10, Germany). The test results were found to comply with the relevant standards. Following solid solution treatment (ST) at 820 °C for 2 h, the Cu-Ni-Be alloy rod achieved a fully homogeneous solid solution state. The inverse pole figure (IPF) map of the alloy is shown in Fig. 1(a). The grain size distribution of the ST Cu-Ni-Be alloy is presented in Fig. 1(b), with an average grain size of 24 µm. The contents of LAGBs and high-angle grain boundaries (HAGBs) were 3 % and 43 %, respectively, while the annealed twin boundary (TB) content was as high as 54 %. Additionally, the grain orientation of the alloy was found to be relatively random, with no distinct texture formation, as illustrated in Fig. 1(c).

The ST Cu-Ni-Be alloy with an initial diameter of 30 mm was subjected to RS deformation at room temperature. Each deformation pass resulted in a 0.3 mm reduction in the diameter of the rod, and after 78 passes, a final wire diameter of 6.7 mm was achieved, corresponding to an equivalent strain (ε) of 3.0 (the sample is named $\mathrm{RS}_{3.0}$). The ε was calculated using the formula $\varepsilon = \ln(A_0/A)$, where A_0 and A represent the initial and final cross-sectional areas, respectively. The $\mathrm{RS}_{3.0}$ sample was further subjected to isothermal aging treatment at temperatures of 573 K, 623, 673 K, 723 K, 773 K, and 873 K for a duration of 1 h, followed by cooling in air. Additionally, to investigate the structural evolution during the RS deformation process, structural characterization was performed on samples with ε of 1.0 and 2.0, which corresponded to diameters of 18.2 mm and 11.0 mm, respectively.

2.2. Mechanical and electrical properties testing

Vickers microhardness tests were performed using an HMV-G 21DT (Shimadzu, Japan) tester with a load of 1.96 N and a dwell time of 10 s in conventional samples. Ten indentations were tested to obtain reliable results.

Quasi-static uniaxial tensile tests were conducted using an AGS-X 10KN universal testing machine (Shimadzu, Japan) at a strain rate of $1 \times 10^{-3}\ \mathrm{s}^{-1}$ and room temperature. Images were recorded at appropriate time intervals for digital image correlation (DIC) analysis. The specimens, with gauge dimensions of 1 mm × 2 mm × 5 mm, were extracted from the core region of the rod.

Electrical conductivity measurements were carried out at 20 °C using a four-point probe resistivity tester. The test specimen measured 0.8 mm × 0.8 mm × 25 mm, with its length oriented along the swaging direction. Conductivity (δ) was determined by the relationship $\delta=1/\rho=RS/l$, where ρ represents resistivity, R is the resistance, S is the cross-sectional area, and l denotes the spacing between the two voltage probes.

2.3. Thermal analysis

Thermal analysis was conducted using a PerkinElmer DSC8000 differential scanning calorimeter (DSC). Polished samples of approximately 30 mg each were sealed in aluminum pans and heated in a nitrogen atmosphere, with an empty aluminum pan used as a reference. Heating rates of 5 K/min, 10 K/min, and 20 K/min were applied to analyze the kinetic parameters during the aging process.

2.4. Microstructural characterizations

X-ray diffraction (XRD) measurements were conducted using a Bruker-AXS D8 diffractometer with Cu Kα radiation. The 2θ angle was scanned from 40° to 100° with a step size of 0.02° and a dwell time of 2 s per step.

Electron backscatter diffraction (EBSD) analysis was conducted using a Zeiss Auriga FIB/SEM coupled with an Oxford Instruments Aztec 2.0 fully automated EBSD system. Sample preparation involved initial polishing with sandpaper, followed by electropolishing on a Buehler ElectroMet@4 using an electrolyte solution of 25 % H_3PO_4, 25 % absolute alcohol, and 50 % deionized water, with an applied voltage of 8 V for 30–60 s. EBSD data processing was performed using Channel5 software.

For transmission electron microscopy (TEM) and scanning transmission electron microscopy (STEM) observations, including bright field (BF) mode and high-angle annular dark field (HAADF) mode, an FEI Titan G2 operating at 300 kV with aberration correction was used. The TEM samples were prepared by machining

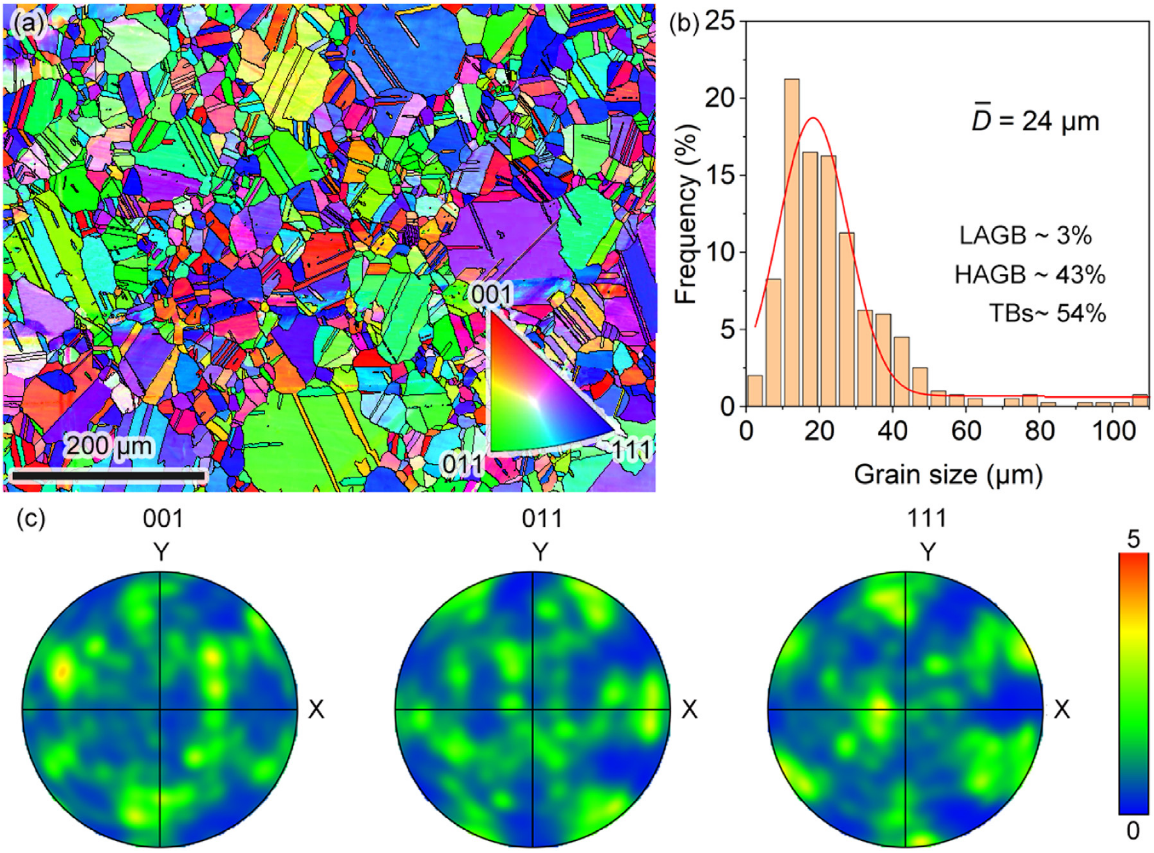

Fig. 1. Microstructure of solid solution coarse-grained Cu-Ni-Be alloy. (a) IPF map, the inset is the legend; (b) grain size distribution; (c) pole figure in (001), (011), and (111) basal plane.

and thinning to 50 μm discs, followed by twin-jet polishing in an electrolyte (25 % H_3PO_4, 25 % absolute alcohol, 50 % deionized water) at approximately 265 K. Residual surface phosphates were removed with ion milling (Gatan 695).

3. Results

3.1. Microstructure evolution of RS process

After RS deformation, the sample, initially a 30 mm diameter rod, was progressively reduced in size. To investigate the mechanisms of deformation and grain refinement, microstructural characterization was performed on intermediate deformation samples with strains $\varepsilon = 1.0$ and $\varepsilon = 2.0$, as shown in Fig. 2. The IPF maps for $\varepsilon = 1.0$ and $\varepsilon = 2.0$ are presented in Fig. 2(a) and (f), respectively. Compared to the ST sample, the grains in both the $\varepsilon = 1.0$ and $\varepsilon = 2.0$ samples are elongated along the axial direction to varying degrees. During deformation, the selective activation of slip systems leads to pronounced grain orientation alignment. The pole figures in Fig. 2(d) and (i) reveal the formation of a strong fiber texture along the axial direction after deformation.

In the pole figure for the {001} crystal family, a distinct preferred grain orientation is evident even at $\varepsilon = 1.0$, with the orientation density concentrated on both sides of *x*-axis. This indicates that during RS, a significant portion of grains have their ⟨001⟩ directions aligned along the rod axis. Similarly, the pole figure for the {111} crystal family shows a comparable trend, with even higher density in the ⟨111⟩ orientation compared to ⟨001⟩. In contrast, the grains in the ⟨011⟩ direction exhibit a dispersed distribution perpendicular to the axis (along *y*-axis direction), which is a result of the axisymmetric nature of the applied stresses and strains during the RS process.

The GBs distribution maps show that at $\varepsilon = 1.0$, the proportion of LAGBs significantly increases, reaching 79 %, while HAGBs and TBs account for only 13 % and 8 %, respectively. As the strain further increases to $\varepsilon = 2.0$, the proportions of LAGBs, HAGBs, and TBs become 72 %, 16 %, and 12 %, respectively, indicating that further deformation induces a gradual transformation of LAGBs into HAGBs, with a small amount of TB formation (Fig. 2(b) and (g)). The average geometrically necessary dislocation (GND) density statistics show values of 5.11×10^{14} m^{-2} and 1.05×10^{15} m^{-2} for the samples at $\varepsilon = 1.0$ and $\varepsilon = 2.0$, respectively, as shown in Fig. 2(c) and (h). Additionally, the average grain widths in the radial direction of the rod were measured, yielding values of 9.89 μm and 4.14 μm for the two samples, respectively.

Continue to increase the ε when it reaches 3.0, the deformed sample, reduced to a diameter of 6.6 mm, exhibits a smooth and shiny surface, as shown in the macroscopic image in Fig. 3(a). This deformation process transformed the initial equiaxed coarse grains into elongated, fiber-like grains aligned parallel to the rod's axis, as illustrated in the metallographic image in Fig. 3(b). Higher-magnification EBSD analysis further revealed that these elongated grains primarily consist of HAGBs, which account for 27 % of the structure. Additionally, LAGBs were observed within the grains, making up 55 % of the structure and also predominantly aligning with the wire axis. The content of TBs decreased from 54 % before deformation to 18 %, and its peak in the misorientation distribution between adjacent grains shifted from 60° of Σ3 to 55°, and most TBs connect with HAGBs, indicating that deformation caused most TBs to lose their coherent relationship and gradually transform into ordinary HAGBs, as shown in the GB map in Fig. 3(d) and the misorientation distribution in Fig. 3(h).

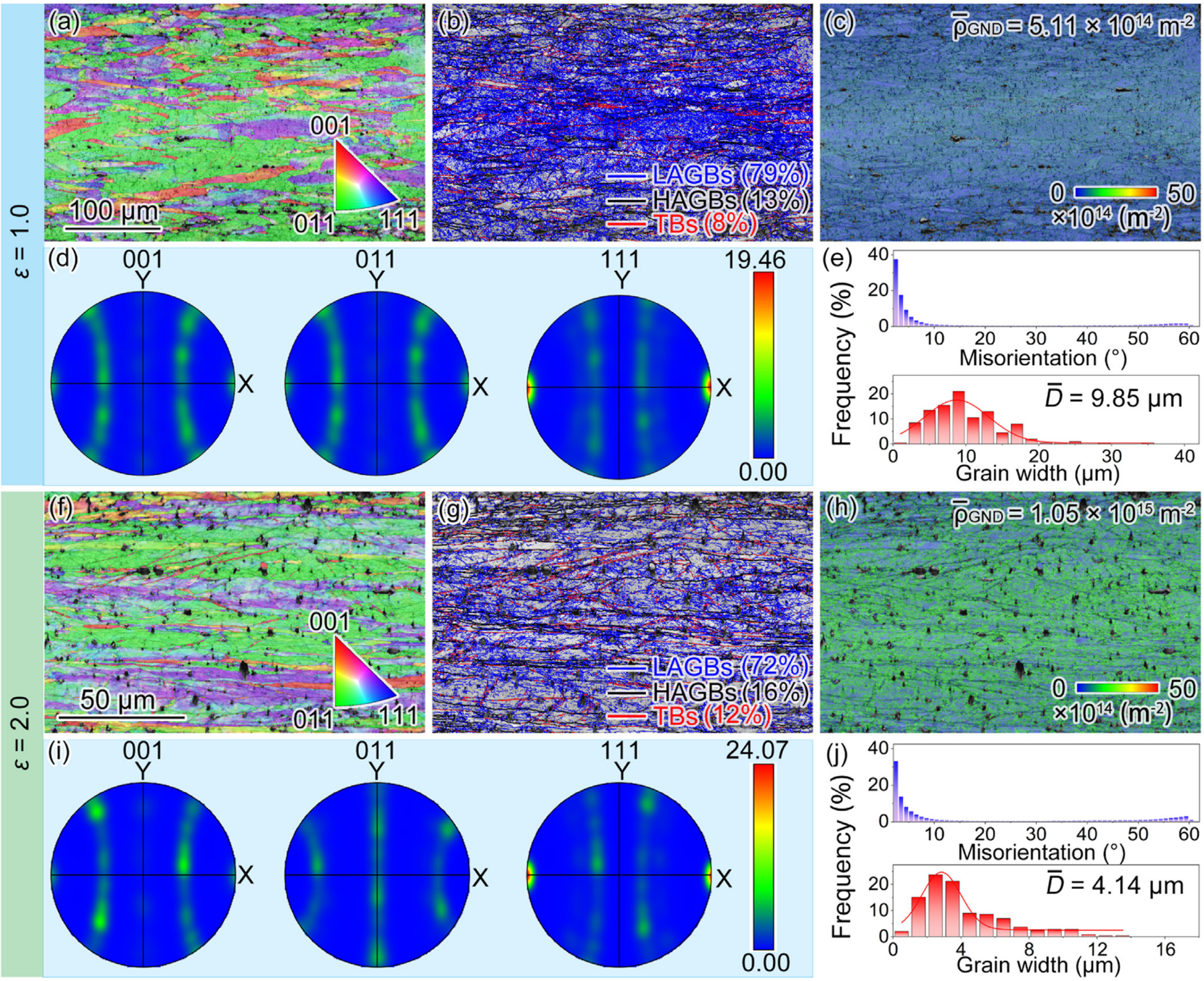

Fig. 2. Microstructure of the samples during the RS process with $\varepsilon = 1.0$ and $\varepsilon = 2.0$. (a) IPF map at $\varepsilon = 1.0$; (b) GB distribution map at $\varepsilon = 1.0$, which includes LAGB (blue line, misorientation < 15°), HAGB (black line, misorientation > 15°), and TB (red line, $\Sigma 3$, fault tolerance angle of 5°); (c) GND map at $\varepsilon = 1.0$; (d) pole figure at $\varepsilon = 1.0$; (e) GB misorientation and grain width distribution at $\varepsilon = 1.0$; (f) IPF map at $\varepsilon = 2.0$; (g) GB map at $\varepsilon = 2.0$; (h) GND map at $\varepsilon = 2.0$; (i) pole figure at $\varepsilon = 2.0$; (j) GB misorientation and grain width distribution at $\varepsilon = 2.0$.

Fig. 3(e) shows that the average GND density was 1.51×10^{15} m^{-2}. Recrystallization mapping (Fig. 3(f)) reveals no evidence of recrystallization in the deformed microstructure, with substructures and deformed grains accounting for 32 % and 68 %, respectively. The $RS_{3.0}$ sample exhibits a texture similar to that of $\varepsilon = 2.0$. Statistical analysis of grain width and axial length, presented in Fig. 3(i) and (j), yielded average values of 0.92 μm and 106 μm, respectively.

Fig. 4 presents the recrystallization distribution maps, GB distribution maps, and GND density distribution maps for the $RS_{3.0}$ samples subjected to aging at 573 K, 673 K, 723 K, 773 K, and 873 K, each for 1 h. Quantitative results from these analyses are further detailed in Fig. 5. In particular, Figs. 4(a1–e1) and 5(a1–e1) show the recrystallized fraction for each condition. For the sample aged at 573 K/1 h, the microstructure primarily comprises 69 % deformed structure and 31 % substructure. At 673 K/1 h, the deformed structure constitutes 67 % of the sample, while the substructure fraction increases to 33 %. Aging at 723 K/1 h results in a further reduction of the deformed structure to 61 %, with 36 % substructure and a small recrystallized fraction of 3 %. At 773 K/1 h, the deformed structure decreases to 41 %, with the substructure at 47 % and recrystallized grains rising to 12 %. Finally, aging at 873 K/1 h produces a microstructure with 58 % recrystallized content, while the deformed structure and substructure are reduced to 28 % and 14 %, respectively.

Fig. 4(a2–e2) displays the GB distribution maps, while Fig. 5(a2–e2) presents the distribution of misorientation angles between adjacent grains, showing the frequency of GBs at different misorientation angles. As the aging temperature increases, the proportion of LAGBs gradually decreases from 57 % at 573 K to 21 % at 873 K. Conversely, the proportion of HAGBs increases from 22 % to 42 %, while the fraction of TBs also shows a progressive rise with temperature, reaching 37 % at the highest temperature of 873 K. This increase in TBs is attributed to the formation of annealing twins associated with recrystallization.

The GND density distribution and statistics are shown in Figs. 4(a3–e3) and 5(a3–e3). The average GND density of the 573 K/1 h sample is 1.48×10^{15} m^{-2}, and for the 673 K/1 h sample, it is 1.46×10^{15} m^{-2}, showing only a slight reduction from the $RS_{3.0}$ and 573 K/1 h conditions, indicating minor dislocation recovery following deformation. With the onset of recrystallization, a more significant decrease in GND density is observed. The 723 K/1 h

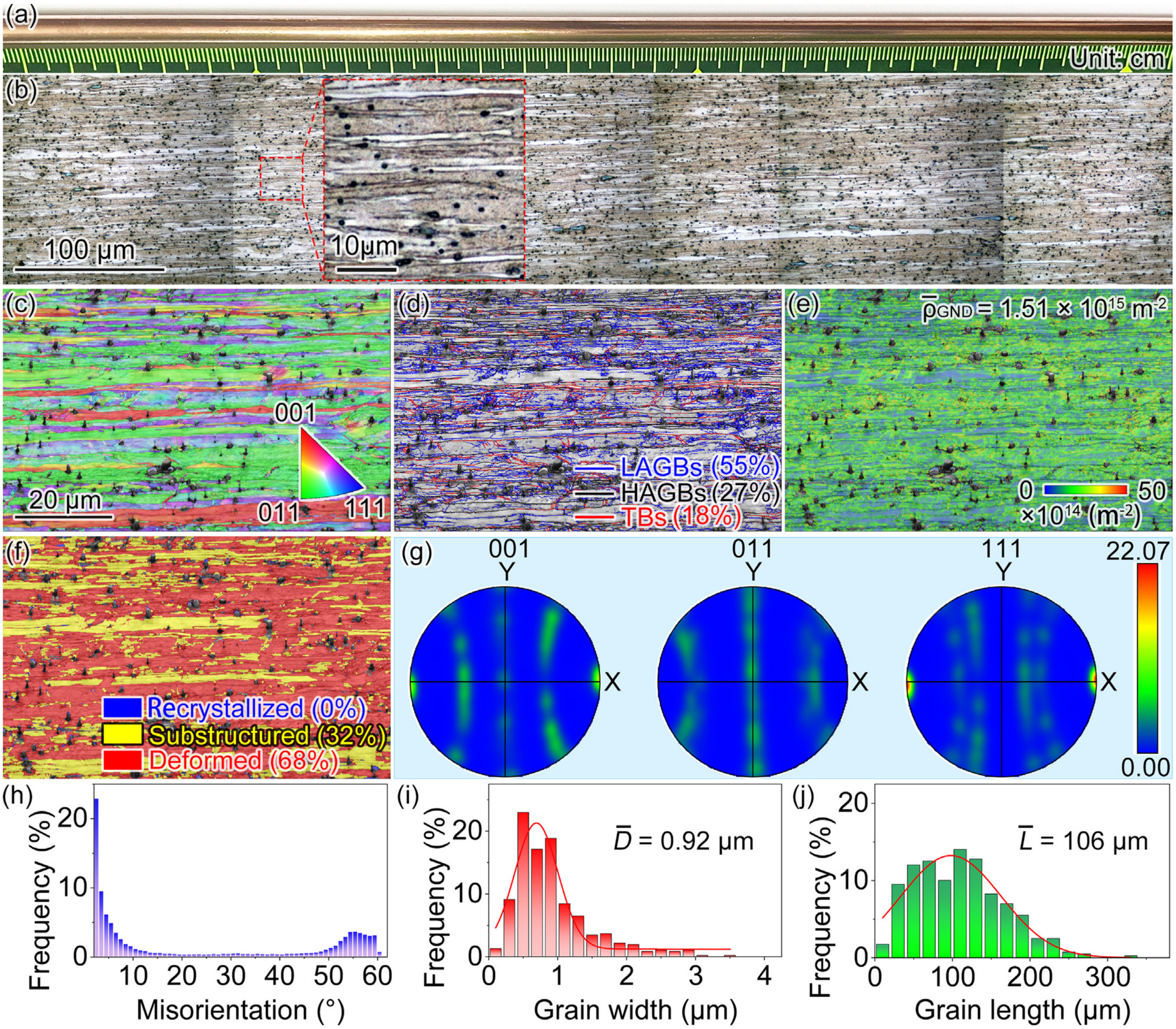

Fig. 3. Macro picture and microstructures of the sample RS$_{3.0}$. (a) Picture of swaged Cu-Ni-Be alloy; (b) metallographic photo; (c) IPF map, inset is the legend; (d) GB map includes LAGBs (blue line, misorientation< 15°), HAGBs (black line, misorientation>15°) and TBs (red line, Σ3, The allowable error angle is 5°); (e) GND map. (f) Recrystallization distribution map; (g) pole figure; (h) GBs misorientation distributions; (i) grain width and (j) grain length statistics.

sample shows a reduced GND density of 1.35×10^{15} m^{-2}. At higher aging temperatures, this trend continues: the 773 K/1 h sample shows a further reduction to 1.16×10^{15} m^{-2}, while the 873 K/1 h sample, with a recrystallized fraction as high as 58 %, exhibits a pronounced drop in GND density to 6.01×10^{14} m^{-2}.

In summary, as the aging temperature increases, recrystallization initiates around 723 K and becomes increasingly prominent at higher temperatures, with the fraction of deformed grains gradually decreasing. The characteristics of the GBs also evolve, with a reduction in LAGBs and a corresponding increase in HAGBs and TBs. Simultaneously, the declining GND density reflects accelerated dislocation elimination and rearrangement with increasing temperature, promoting material softening and texture adjustment. These microstructural changes have a direct impact on the material's mechanical properties, particularly its strength and ductility, this will be introduced in the following text.

Associated with the recrystallization occurring and fraction increases, the texture of materials also undergoes notable changes, the pole density of grains oriented along the ⟨111⟩ axis decreases, while the pole density of <001>-oriented grains increases. Despite the occurrence of recrystallization, the sample predominantly retains the ⟨001⟩ and ⟨111⟩ fiber textures, as shown in Fig. 6. This texture inheritance is due to the influence of internal dislocation structures, sub-grain structures, and dislocation densities formed during deformation, which directly impacts the nucleation and growth of grains during recrystallization. Certain orientations within the deformed texture more readily form new grains during recrystallization, resulting in a preferential nucleation and growth process that preserves aspects of the original texture.

In Fig. 3(d), a large number of LAGBs were observed within the grains, and the length direction of the sub-grains composed of LAGBs is consistent with the length direction of the grains composed of HAGBs. Further examination using STEM-BF imaging revealed that the sub-grains within the grains of the RS$_{3.0}$ sample had an average width of approximately 200 nm, with a high dislocation density inside (Fig. 7(a)), therefore, a typical fractal structure composed of metal wires, grain fibers, and sub-grain fibers was constructed by RS. For the sample aged at 673 K for 1 h, no significant change in the average width of the sub-grains was observed. In contrast to the RS$_{3.0}$ sample, the dislocation density within the sub-grains of the aged sample was reduced, as shown in Fig. 7(b).

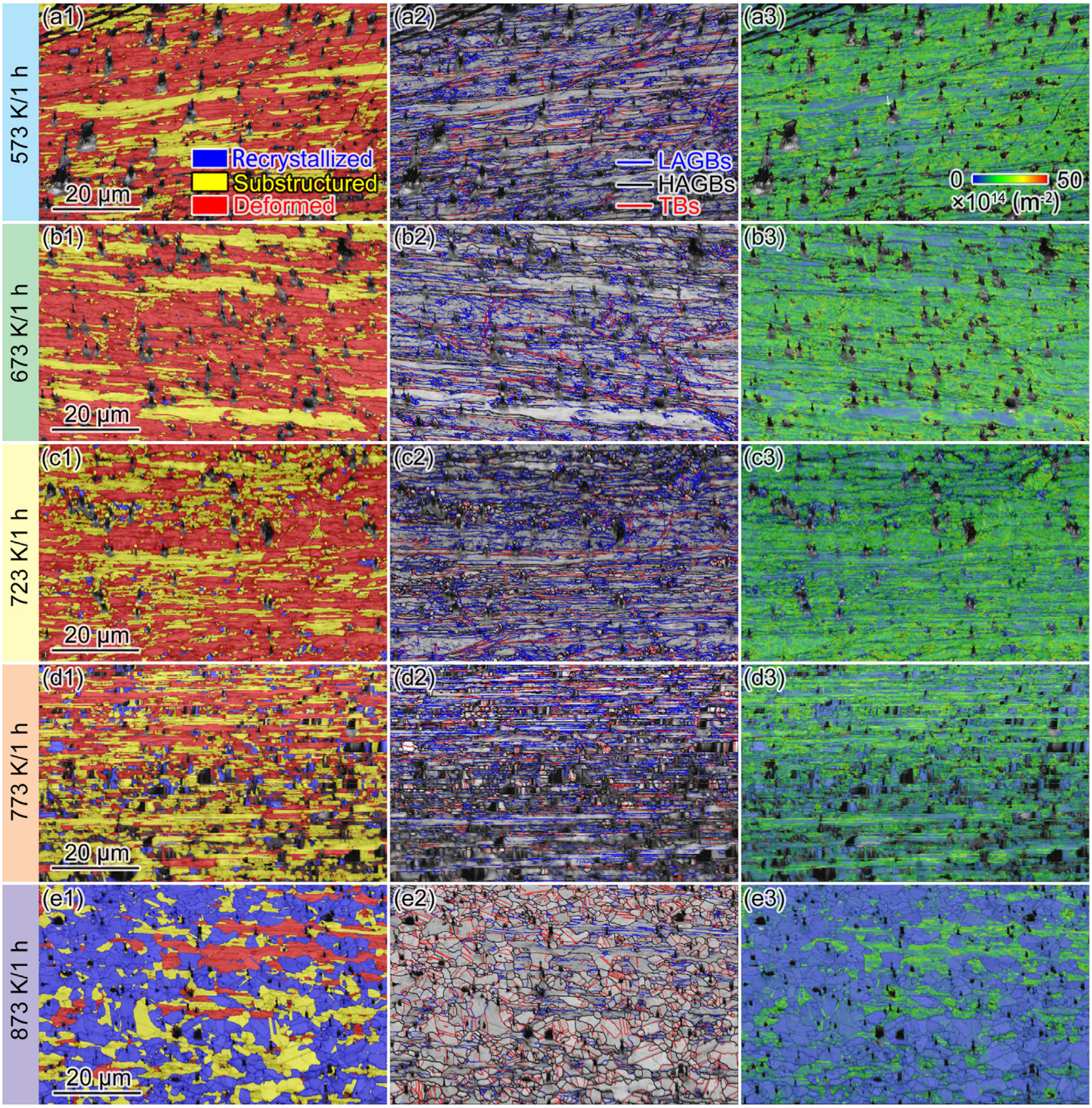

Fig. 4. Recrystallization distribution maps (a1, b1, c1, d1, e1), GBs distribution maps (a2, b2, c2, d2, e2), and GND density distribution maps (a3, b3, c3, d3, e3) of $RS_{3.0}$ after aging at: (a1, a2, a3) 573 K/1 h, (b1, b2, b3) 673 K/1 h, (c1, c2, c3) 723 K/1 h, (d1, d2, d3), 773 K/1 h; (e1, e2, e3) 873 K/1 h.

3.2. Precipitation behavior

The XRD curves of the Cu-Ni-Be alloy after RS and subsequent aging are shown in Fig. 8(a). The side view of the $RS_{3.0}$ round sample exhibits a pronounced {220} diffraction peak and a relatively weaker {200} diffraction peak, along with very weak {111} and {311} diffraction peaks. This result is consistent with the IPF results in Figs. 3 and 6, indicating that the low-temperature aging does not significantly alter this texture composition. However, at an aging temperature of 723 K, there is a slight increase in the intensities of the {111} and {311} peaks, a trend that becomes more pronounced at higher aging temperatures. This observation aligns with the recrystallization distribution maps in Fig. 4, confirming the onset of recrystallization in samples aged at 723 K and above.

Additionally, aging leads to a shift in the diffraction peaks, attributed to changes in the lattice constant (a). Nelson extrapolation function $f(\theta)$ is used to estimate the value of a [25]:

$$f(\theta) = \frac{1}{2}\left(\frac{\cos^2\theta}{\sin\theta} + \frac{\cos^2\theta}{\theta}\right) \tag{1}$$

where θ is the half Bragg angle, from the different diffraction peak angles obtained by XRD curves, and a is the intercept obtained from the linear fitting of $f(\theta)$ versus θ. The results indicate that the precipitation of Be atoms from the saturated solid solution increases the a of the alloy. This effect is due to the atomic radius

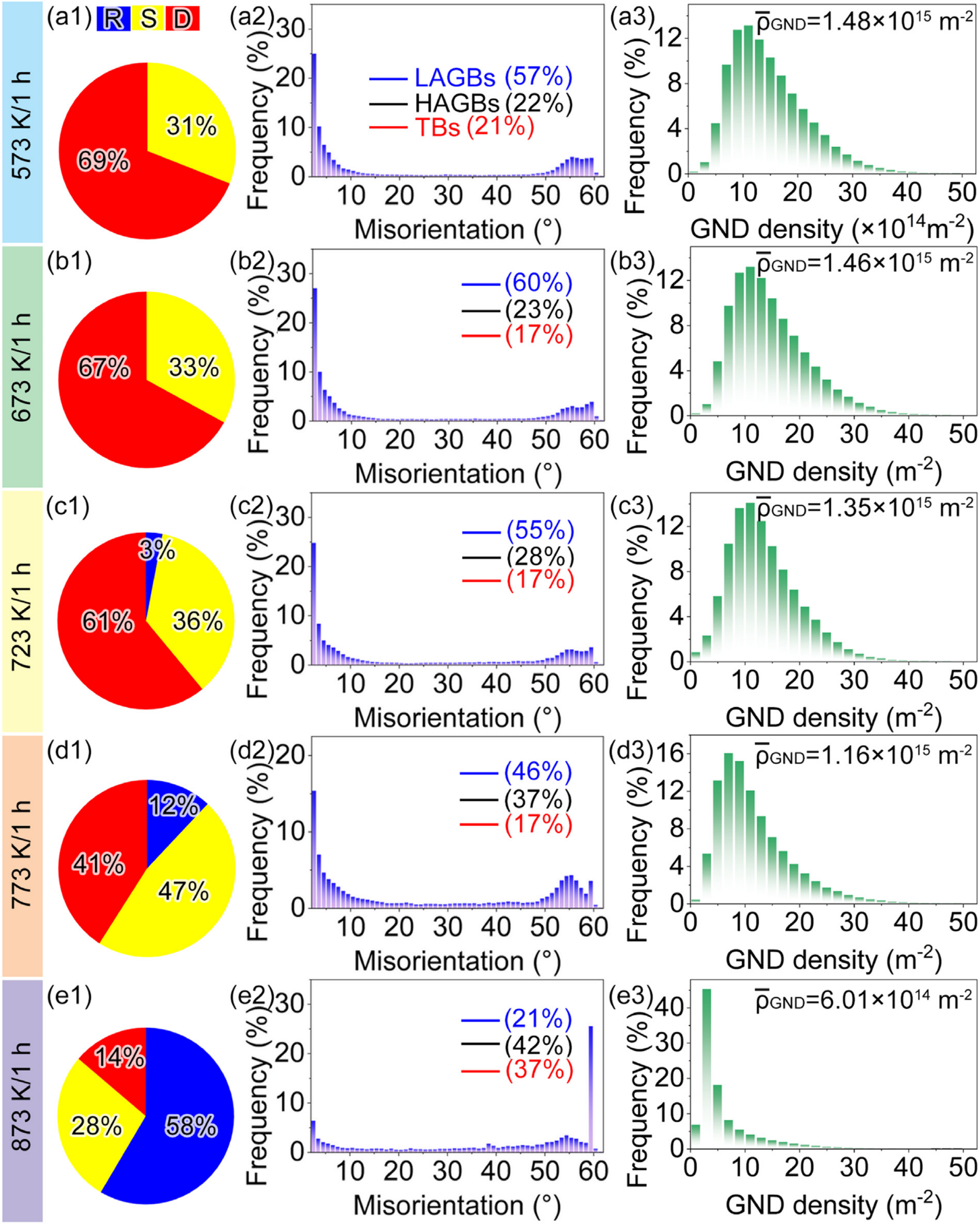

Fig. 5. Statistics of recrystallization content (a1, b1, c1, d1, e1), misorientation (a2, b2, c2, d2, e2), and GND density (a3, b3, c3, d3, e3) of RS$_{3.0}$ samples after annealing at: (a1, a2, a3) 573 K/1 h, (b1, b2, b3) 673 K/1 h, (c1, c2, c3) 723 K/1 h, (d1, d2, d3), 773 K/1 h, and (e1, e2, e3) 873 K/1 h. "R", "S", and "D" represent recrystallization, substructure, and deformation, respectively.

of Be (112 pm) being smaller than that of the Cu matrix (128 pm) when Be atoms are present in a substitutional solid solution. Consequently, Be dissolution in the Cu matrix induces lattice distortion, reducing the lattice constant, while Be precipitation increases it.

The lattice constant of the 573 K/1 h sample is similar to that of the RS$_{3.0}$ sample (0.3603 nm), suggesting minimal Be precipitation at this temperature. In contrast, the lattice constants of the 623 K/1 h and 673 K/1 h samples show progressive increases (0.3605 nm and 0.3609 nm, respectively). For samples aged above

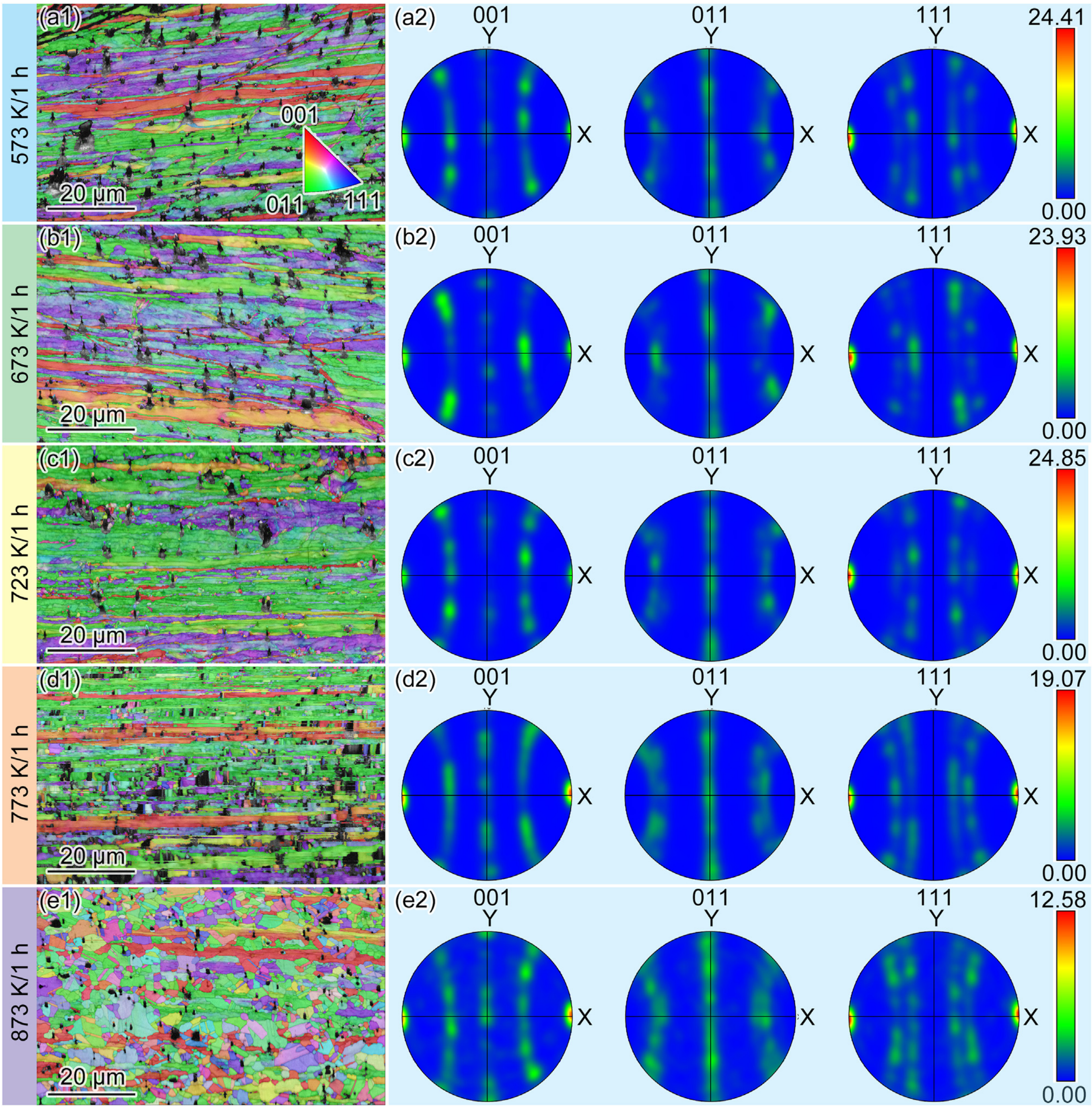

Fig. 6. IPF map (a1, b1, c1, d1, e1) and pole figure (a2, b2, c2, d2, e2) of $RS_{3.0}$ sample after annealing at: (a1, a2) 573 k/1 h; (b1, b2) 673 K/1 h; (c1, c2) 723 K/1 h; (d1, d2) 773 K/1 h; (e1, e2) 873 K/1 h.

673 K, the lattice constant stabilizes at 0.3610 nm, indicating that Be precipitation has reached equilibrium in these samples.

During the aging process of Cu-Be, Cu-Ni-Be, and Cu-Co-Be alloys, the precipitation sequence is generally considered to proceed as follows: Cu-based supersaturated solid solution, Guinier-Preston (G.P.) zones, γ'', γ', and finally γ. The G.P. zones consist of single layers of Be atoms parallel to the (001) plane of the α-Cu matrix, forming in the early stages of aging [26]. The γ'' precipitates are disk-shaped and maintain a coherent relationship with the α-Cu matrix, growing further along their wide face parallel to the 001 plane of the α-Cu matrix, with Ni atoms enriched around the Be monolayers [27], this coherency allows the γ'' phase to initially integrate smoothly into the Cu matrix, with its lattice planes and orientations well-aligned with those of the matrix, thereby reducing interfacial energy. However, as the size of the γ'' precipitates increases or the aging time is extended, the coherency may gradually diminish. The γ' phase is also disk-shaped but is semi-coherent with the α-Cu matrix [28] and larger than the γ'' phase. With sufficient aging time or elevated temperatures, the γ' precipitates are eventually replaced by the stable γ phase [29].

Metastable phases typically exhibit a more dispersed distribution and smaller size, which significantly enhance the material's strength compared to stable phases. In this study, both the ST and $RS_{3.0}$ samples achieved their maximum yield strength after aging at 673 K for 1 h (as shown in Fig. 11 in the following text). Therefore, the precipitates microstructure of the $RS_{3.0}$–673 K/1 h sample was characterized to further investigate the strengthening mechanism. Fig. 9(a) presents the high-resolution TEM (HRTEM) image of the 673 K/1 h sample. Following aging, numerous precipitates have separated from the matrix. Based on the FFT image in Fig. 9(d),

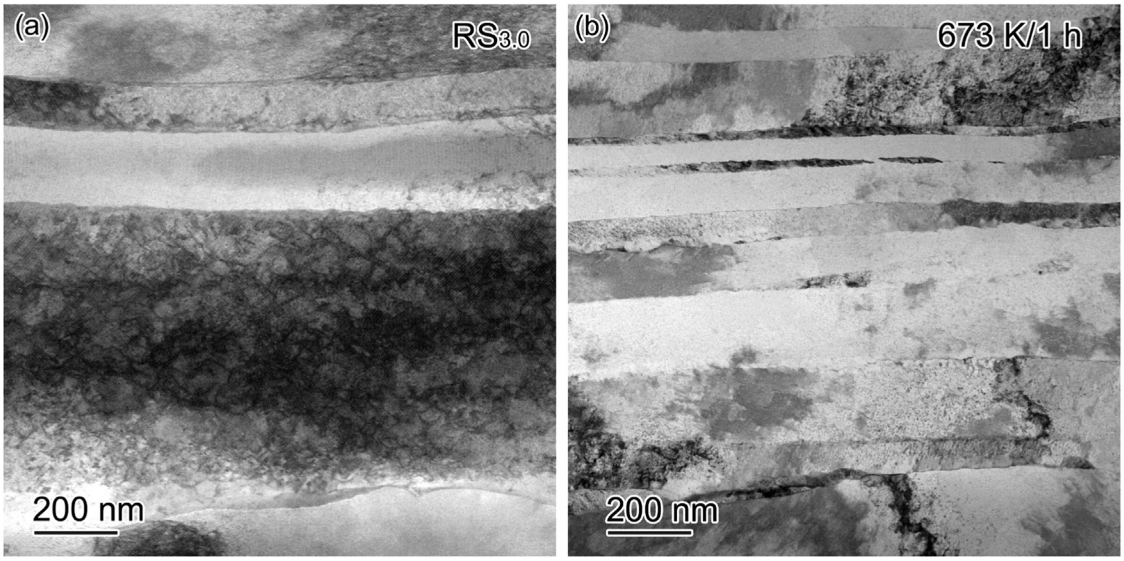

Fig. 7. STEM-BF images of the interior of the grains. (a) $RS_{3.0}$; (b) $RS_{3.0}$–673 K/1 h.

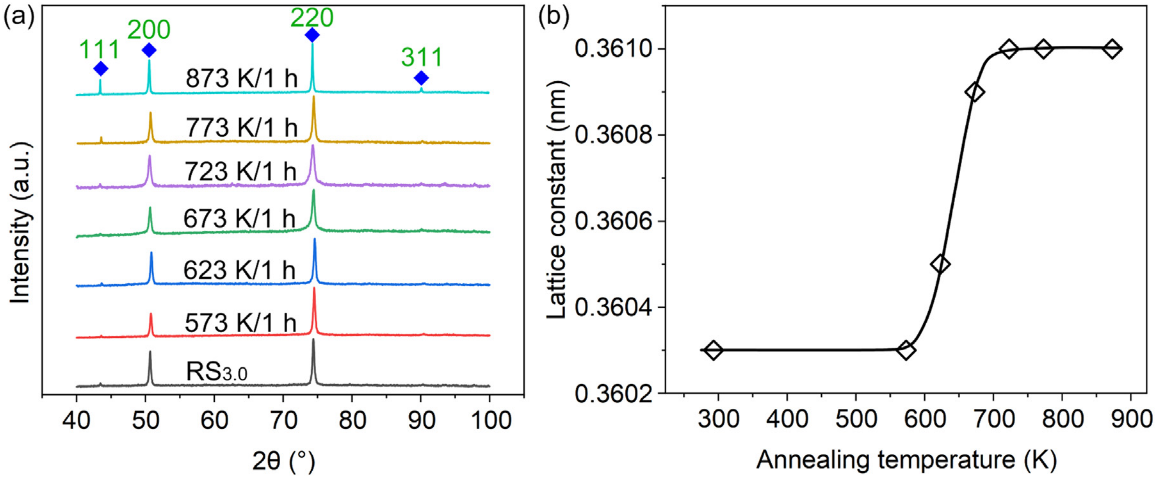

Fig. 8. XRD curves and lattice constant estimation based on XRD curves of Cu-Ni-Be alloy in RS and subsequent aging state. (a) XRD curves; (b) lattice constant.

the precipitate phase is identified as γ''. The red box in Fig. 9(a) highlights a region magnified in Fig. 9(b), and the intensity profile along the dotted line is shown in Fig. 9(c). The weaker diffraction contrast observed is attributed to the presence of lighter Be atoms. Fig. 9(c) also shows the FFT reciprocal lattice image of an individual γ'' phase, where additional patterns appear at the 1/2(220) positions compared to the matrix. The elongated γ'' precipitates are aligned parallel to the (002) plane of the Cu matrix, with the orientation relationship described as $[100]_p//[110]_M$, consistent with the classic Bain relationship for FCC/BCC structures. Fig. 9(e) shows the IFFT image of selected spots from the inset, revealing slight lattice distortion surrounding the coherent γ'' phase. This lattice distortion is further visualized in the geometric phase analysis (GPA) map shown in Fig. 9(f).

3.3. Mechanical and electrical properties

The hardness distribution along the diameter of the cross-section of the $RS_{3.0}$ sample is shown in Fig. 10. The hardness stabilizes at approximately 180 HV in the region radially located >1.5 mm from the center. However, within a 3 mm diameter at the core, the hardness exhibits a gradient pattern, with the highest hardness at the center (up to 208 HV) gradually decreasing towards the periphery. This continuous hardness gradient in the swaged Cu-Ni-Be alloy resembles that observed in swaged pure copper [11], suggesting that dislocation slip remains the dominant deformation mechanism for this high stacking-fault energy alloy during RS, rather than extensive twinning [30]. Given the minor property differences between the core and edge, the material can be considered relatively homogeneous, and samples for performance testing and microstructural characterization were extracted from the very center of the wire to ensure comparability.

During subsequent aging, the processes of dislocation recovery, precipitate formation, and recrystallization become prominent. At 573 K/1 h, the hardness distribution remains similar to the as-swaged state. At 623 K/1 h and 673 K/1 h, the hardness of the alloy significantly increases while retaining the gradient distribution: at 623 K/1 h, core hardness reaches 240 HV, and edge hardness is 217 HV; at 673 K/1 h, core hardness reaches 278 HV, and edge hardness is 262 HV. At higher aging temperatures (773 K/1 h and 873 K/1 h), both the core and edge hardness are markedly reduced compared to the 673 K/1 h condition, and the hardness difference between the core and edge is nearly eliminated, primarily due to recrystallization.

In this study, quasi-static tensile tests at room temperature were conducted to systematically analyze the mechanical proper-

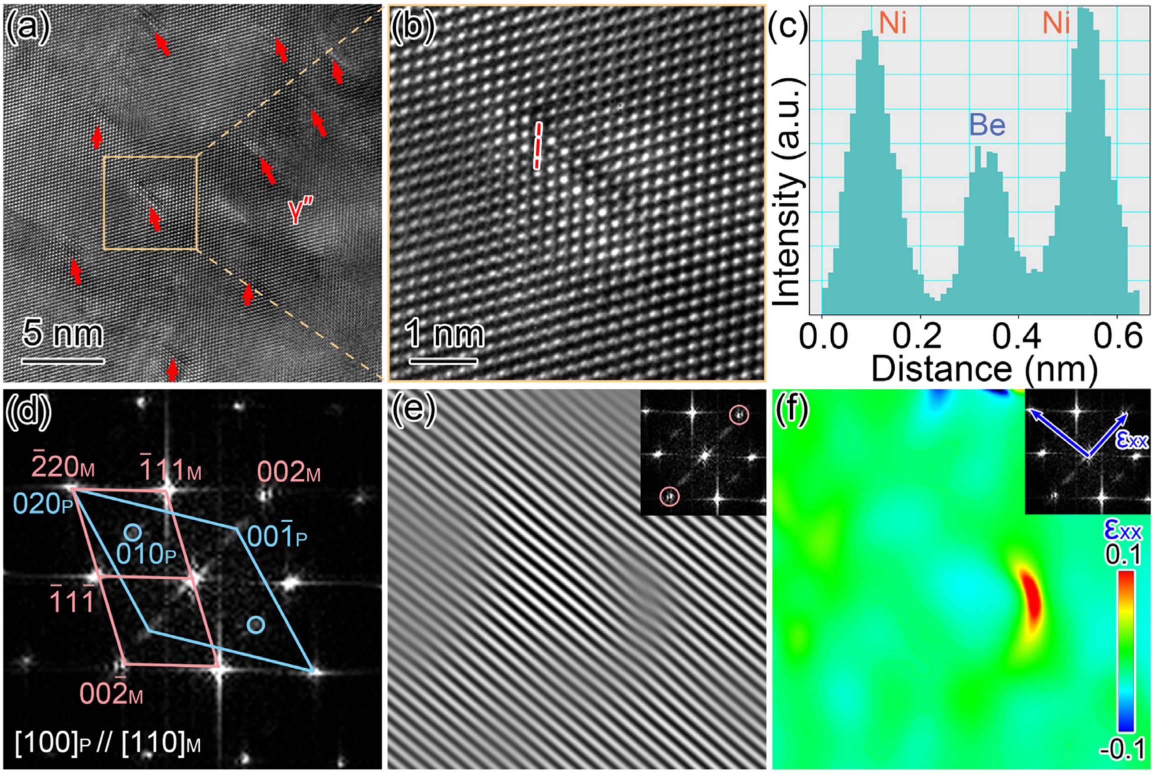

Fig. 9. Precipitates structure of $RS_{3.0}$–673 K/1 h sample. (a) HRTEM; (b) enlarged image within the yellow box in (a); (c) the one-dimensional intensity distribution at the red dashed line in (b); (d) FFT image of (b); (e) IFFT image-based on the pink circle shown in the inset in (e); (f) geometrical phase analysis (GPA) image based on the vector ε_{xx} shown in the inset in (f).

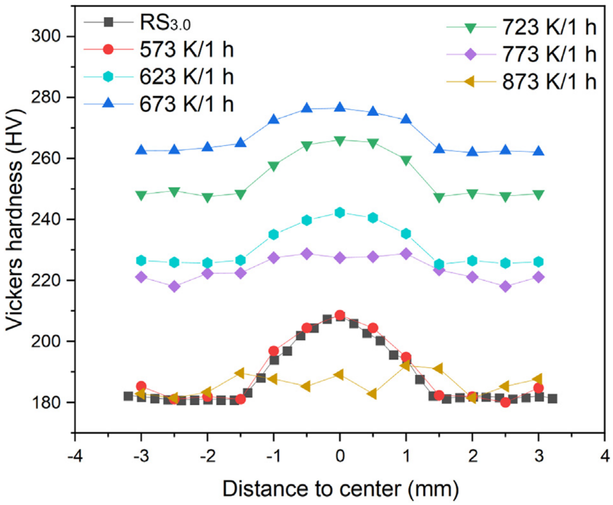

Fig. 10. Radial hardness distribution of samples after RS and subsequent annealing.

Table 2
Yield strength $\sigma_{0.2}$, UTS, uniform elongation ε_u, and elongation to fracture ε_f of ST and $RS_{3.0}$ samples and their subsequent aging treated samples.

Samples	$\sigma_{0.2}$ (MPa)	UTS (MPa)	ε_u (%)	ε_f (%)
ST	100	314	34.8	50.8
ST-573 K/1 h	107	354	31.2	45.1
ST-623 K/1 h	377	571	21.5	34.6
ST-673 K/1 h	572	757	18.7	26.2
ST-723 K/1 h	526	766	20.3	24.9
ST-773 K/1 h	518	723	17.7	23.9
ST-873 K/1 h	390	517	13.1	26.8
$RS_{3.0}$	698	706	1.4	9.7
$RS_{3.0}$–573 K/1 h	680	712	7.6	14.5
$RS_{3.0}$–623 K/1 h	776	848	10.2	14.1
$RS_{3.0}$–673 K/1 h	962	1064	10.4	16.1
$RS_{3.0}$–723 K/1 h	879	974	11.3	15.7
$RS_{3.0}$–773 K/1 h	697	785	9.7	17.1
$RS_{3.0}$–873 K/1 h	305	461	16.2	33.0

ties of $RS_{3.0}$ samples under various aging conditions, the same aging conditions were also applied to ST samples for comparison, as shown in Fig. 11. For the ST sample, the unaged condition exhibited a yield strength ($\sigma_{0.2}$) of 100 MPa, ultimate tensile strength (UTS) of 314 MPa, uniform elongation (ε_u) of 34.8 %, and elongation to fracture (ε_f) of 50.8 %. Aging at 673 K for 1 h resulted in the maximum $\sigma_{0.2}$ (572 MPa), but at the cost of reduced ductility, with ε_u decreasing to 18.7 %. At a higher aging temperature of 873 K for 1 h, $\sigma_{0.2}$ and ε_u significantly decreased to 390 MPa and 13.1 % simultaneously.

For the $RS_{3.0}$ sample, the unaged condition showed high strength, with $\sigma_{0.2}$ of 698 MPa and UTS of 706 MPa, but low ductility (ε_u = 1.4 %, ε_f = 9.7 %). Aging at 673 K for 1 h resulted in the highest strength, with $\sigma_{0.2}$ reaching 962 MPa and UTS reaching 1064 MPa, while ε_u and ε_f were 10.4 % and 16.1 %. However, at 873 K for 1 h, $\sigma_{0.2}$ and UTS decreased to 305 MPa and 461 MPa, with a significant increase in ductility, as ε_u and ε_f improved to 16.2 % and 33.0 %, respectively. The $\sigma_{0.2}$, UTS, ε_u, and ε_f of ST and $RS_{3.0}$ samples and their aging treated samples are shown in Table 2.

Fig. 12 presents the DIC results for the samples $RS_{3.0}$ and 673 K/1 h. Consistent with the tensile curves, the $RS_{3.0}$ sample exhibits uniform deformation only up to about 1.0 % strain, with pronounced macroscopic shear bands forming across the specimen at 3 % strain, leading to local necking. This behavior indicates that the $RS_{3.0}$ sample loses its ability to sustain uniform deformation at rel-

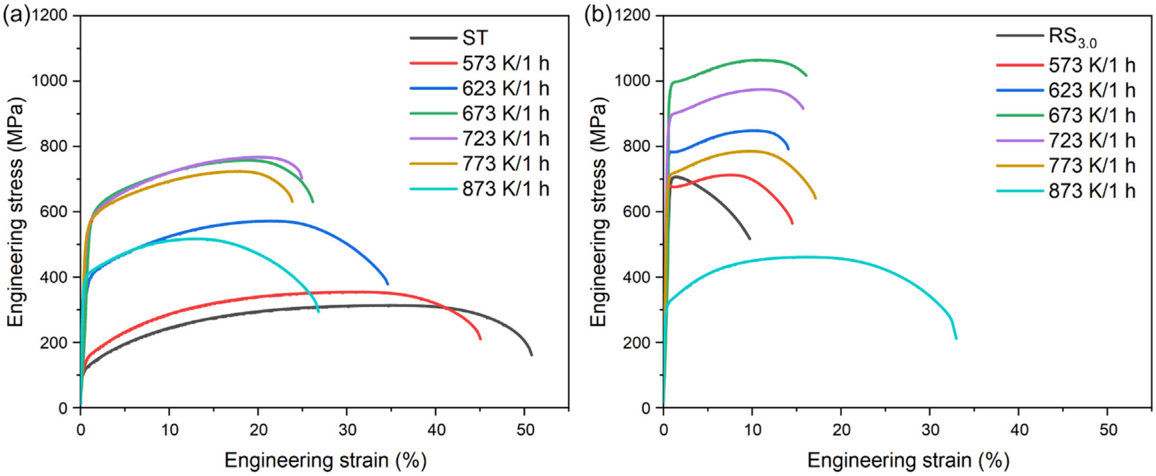

Fig. 11. Quasi-static tensile curves. (a) Solid solution and subsequent aging state. (b) Swaging state after solid solution and subsequent aging state.

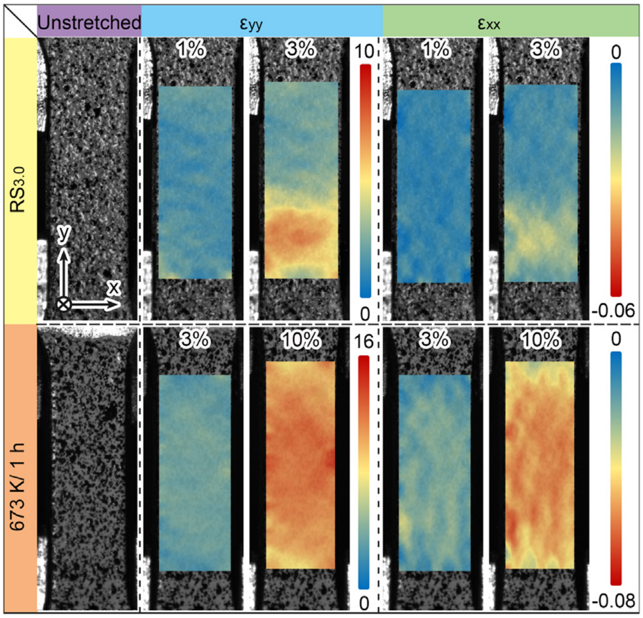

Fig. 12. DIC results of $RS_{3.0}$ and $RS_{3.0}$–673 K/1 h sample.

atively low strains, rapidly transitioning to non-uniform deformation. This transition causes significant stress concentration in localized areas, promoting the formation of macroscopic shear bands and early failure of the material.

In contrast, the 673 K/1 h sample demonstrates superior deformation capacity. At an early tensile strain of 3 %, the sample maintains uniform deformation, and as the strain increases to 10 %, the formation and dispersion of wavy microscopic shear bands are observed. These wavy shear bands play a crucial role in enhancing the deformation ability of the 673 K/1 h sample. They effectively distribute stress across the material, alleviating stress concentration in localized areas and thereby delaying the onset of necking.

Due to the near-zero solubility of Be atoms in the Cu matrix at room temperature, Cu-Ni-Be alloys can undergo aging to precipitate Be atoms, thereby optimizing conductivity and making these alloys suitable as high-strength and high-conductivity materials. In this study, the electrical conductivity of both ST and $RS_{3.0}$ samples was analyzed under various aging treatments, as shown in Fig. 13.

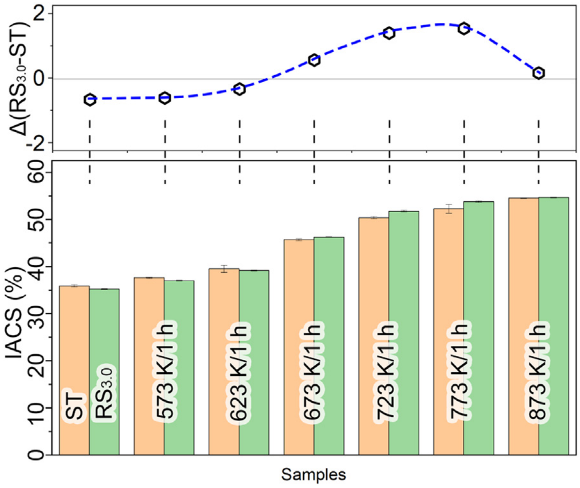

Fig. 13. Conductivity of ST and $RS_{3.0}$ and their aged state samples.

For the unaged samples, the conductivity of the ST sample was 35.9 % international annealed copper standard (IACS), while that of the $RS_{3.0}$ sample was 35.2 % IACS, showing a close initial similarity. With increasing aging temperature, the conductivity of the ST sample gradually increased: reaching 37.6 % IACS at 573 K/1 h, and 39.5 % IACS at 623 K/1 h. When aged at 673 K/1 h, the conductivity of the ST sample rose significantly to 45.7 % IACS and further increased to 50.4 % IACS at 723 K/1 h. At 773 K/1 h, the conductivity reached 52.3 % IACS, ultimately attaining a peak value of 54.5 % IACS at 873 K/1 h.

The $RS_{3.0}$ sample displayed a similar trend in conductivity but was generally slightly higher than the ST sample. Following aging at 573 K/1 h, the conductivity of the $RS_{3.0}$ sample rose to 37.0 % IACS, further increasing to 39.2 % IACS at 623 K/1 h. At 673 K/1 h, the conductivity reached 46.3 % IACS, surpassing that of the ST sample. The conductivity continued to increase to 51.8 % IACS at 723 K/1 h and to 53.8 % IACS at 773 K/1 h, eventually reaching 54.7 % IACS at 873 K/1 h, slightly higher than the ST sample's 54.5 % IACS.

To explore conductivity differences between these two processing methods, the conductivity difference between $RS_{3.0}$ and ST samples was calculated as $\Delta(RS_{3.0}\text{–}ST)$ for each unaged and aged condition, as shown in the upper part of Fig. 13. The results indicate that for aging temperatures below 623 K, the conductivity of the deformed $RS_{3.0}$ sample was lower than that of the ST sample under the same conditions, likely due to the high density of dislocations introduced by deformation. However, for aging temperatures at or above 673 K, the conductivity of the $RS_{3.0}$ sample exceeded that of the ST sample, likely due to dislocation recovery and the influence of grain shape. At the highest aging temperature of 873 K, both samples exhibited similar conductivity, as the $RS_{3.0}$ sample had undergone extensive recrystallization.

4. Discussion

4.1. Precipitation kinetics

During the formation of precipitates, the nucleation and growth processes can be explained by changes in system energy. As a new phase precipitates from a supersaturated solid solution, free energy is released. This occurs because the system transitions from a high-energy state (supersaturated solid solution) to a lower-energy state (solid solution with precipitates). This reaction requires overcoming an initial nucleation energy barrier, meaning that the precipitation process has an associated activation energy (Q). The magnitude of this activation energy influences the kinetics of the precipitation reaction; a higher activation energy indicates that a higher temperature or longer time is required for the process to occur.

In the continuous heating DSC tests, the transformation percentage (Y) as a function of time (t) and temperature can be described as follows [31]:

$$\frac{\mathrm{d}Y}{\mathrm{d}t} = \frac{\mathrm{d}Y}{\mathrm{d}T} \cdot \varphi \tag{2}$$

According to the modified JMAK equation [32]:

$$Y = 1 - \exp\left(-k^n t^n\right) \tag{3}$$

where n is a parameter depending on nucleation density and growth mode of the precipitate phase, and k is the rate constant, defined as:

$$k = k_0 \exp(-Q/RT) \tag{4}$$

where T is the temperature, R is the gas constant (8.314 J/(mol K)), and k_0 is a constant related to the rate constant. For non-isothermal transformations, the transformation rate can be expressed as

$$\frac{\mathrm{d}(Y)}{\mathrm{d}(t)} = K(T)f(Y) \tag{5}$$

where $f(Y)$ is an implicit function of Y as described in Eq. (3). By combining the derivative of Eq. (2) with Eq. (5):

$$f(Y) = n(1-Y)\left[-\ln(1-Y\right]^{(n-1)/n} \tag{6}$$

The non-isothermal kinetic data obtained from DSC analysis in Eq. (2) can be written as:

$$\frac{\mathrm{d}(Y)}{\mathrm{d}(T)} = \frac{1}{\varphi}\frac{\mathrm{d}(Y)}{\mathrm{d}(t)} = \frac{1}{\varphi}K(T)f(Y) \tag{7}$$

Combine Eqs. (2), (6), and (7) to yield:

$$\ln[\left(\mathrm{d}Y/\mathrm{d}T\right) \cdot \left(\varphi/f(Y)\right)] = \ln k_0 - (Q/R)(1/T) \tag{8}$$

Assuming that n remains constant during the reaction, an iterative approach can be used to test values of n until the linear fit error of $\ln[(\mathrm{d}Y/\mathrm{d}T) \cdot (\varphi/f(Y))]$ vs $1/T$ is minimized. The optimal n value, along with the slope $-Q/R$ and intercept $\ln k_0$, allows for the determination of Q and k_0.

The DSC curves of the precipitation reactions for ST and $RS_{3.0}$ samples at different heating rates are shown in Fig. 14(a). With increasing heating rates, both the peak area and peak temperature shift to higher values. By integrating the peak area and normalizing it, the Y as a function of T can be obtained, as illustrated in Fig. 14(b). According to Eq. (8), plotting $\ln[(\mathrm{d}Y/\mathrm{d}T) \cdot (\varphi/f(Y))]$ versus $1/T$ and performing linear fitting yields slopes of -18.2244 and -18.0580 for the ST and $RS_{3.0}$ samples, respectively. The calculated Q for the two samples are 151.5 kJ/mol and 150.1 kJ/mol, as shown in Fig. 14(c). Based on Eqs. (3) and (4), the Y value at specific T and t can be estimated (Fig. 14(d)).

Table 3
Enthalpy changes (ΔH) for the ST and $RS_{3.0}$ samples during the precipitation process.

Samples	ΔH (J/g)
ST	-8.7 ± 1.3
$RS_{3.0}$	-8.8 ± 2.2

The enthalpy changes (ΔH) corresponding to the exothermic peaks in the DSC curves are summarized in Table 3. The two samples exhibit similar ΔH (-8.7 ± 1.3 J/g for ST and -8.8 ± 2.2 J/g for $RS_{3.0}$), indicating that under sufficient aging conditions, solutes can be effectively dissolved. Additionally, the Q and the n values for both samples are very similar, indicating that the energy barriers to be overcome during aging and the nucleation density and growth modes of the precipitate phases are similar.

However, a noticeable difference is observed in the k_0, with the k_0 value for the ST sample being 1.6 times higher than that for $RS_{3.0}$. This difference results in more complete solute precipitation in the ST sample during the precipitation process, compared to the $RS_{3.0}$ sample, under the same aging conditions.

To reveal the differences in the precipitation processes between the two samples, the microstructure of both samples after aging at 673 K for 1 h was characterized, as shown in Fig. 15. Both alloys exhibit a dispersed distribution of nanometer-sized precipitates within the grains, with similar densities. The difference lies in the average precipitate size: Sample ST-673 K/1 h shows a larger average precipitate size (2.1 nm), while Sample $RS_{3.0}$–673 K/1 h presents smaller precipitates (1.6 nm). Considering that aging at 673 K for 1 h does not result in complete phase transformation in the alloys (Fig. 14(d)), this could be attributed to the precipitation delay in the $RS_{3.0}$–673 K/1 h sample, due to its lower k_0 value.

Previous studies have shown that plastic deformation significantly affects precipitation. For example, in the case of 7075 Al alloy, the precipitation kinetics were accelerated by equal channel angular pressing, allowing precipitation to occur at lower temperatures compared to the solution-treated alloy [33]. A similar phenomenon was observed in Al-2 wt %Cu alloy produced by accumulation of rolling bonding [34], where deformation-induced GBs and dislocations provided additional nucleation sites for precipitation. However, for some alloys, deformation may inhibit precipitation. For instance, in Ni-Ti shape memory alloys, the NC and ultrafine-grained structures hinder precipitation due to geometric constraints [35], and in Al-Mg alloys, segregation due to deformation can prevent the formation of the equilibrium Al_3Mg_2 phase [36]. In conclusion, precipitation behavior is influenced by various factors such as temperature, time, composition, dislocations, GBs, and stress fields.

Considering that the $RS_{3.0}$ sample has a much higher density of GBs and dislocations compared to the ST sample, yet both samples exhibit similar Q, n, and ΔH values, it suggests that in RS Cu-Ni-Be alloys, precipitation behavior is not sensitive to the nucleation sites provided by GBs and dislocations. Previous studies have demonstrated that vacancies significantly influence precipitation behavior, with thermal activation affecting vacancy concentration as follows [37]:

$$c = A \cdot \exp\left(-\frac{E_f}{k_B T}\right) \tag{9}$$

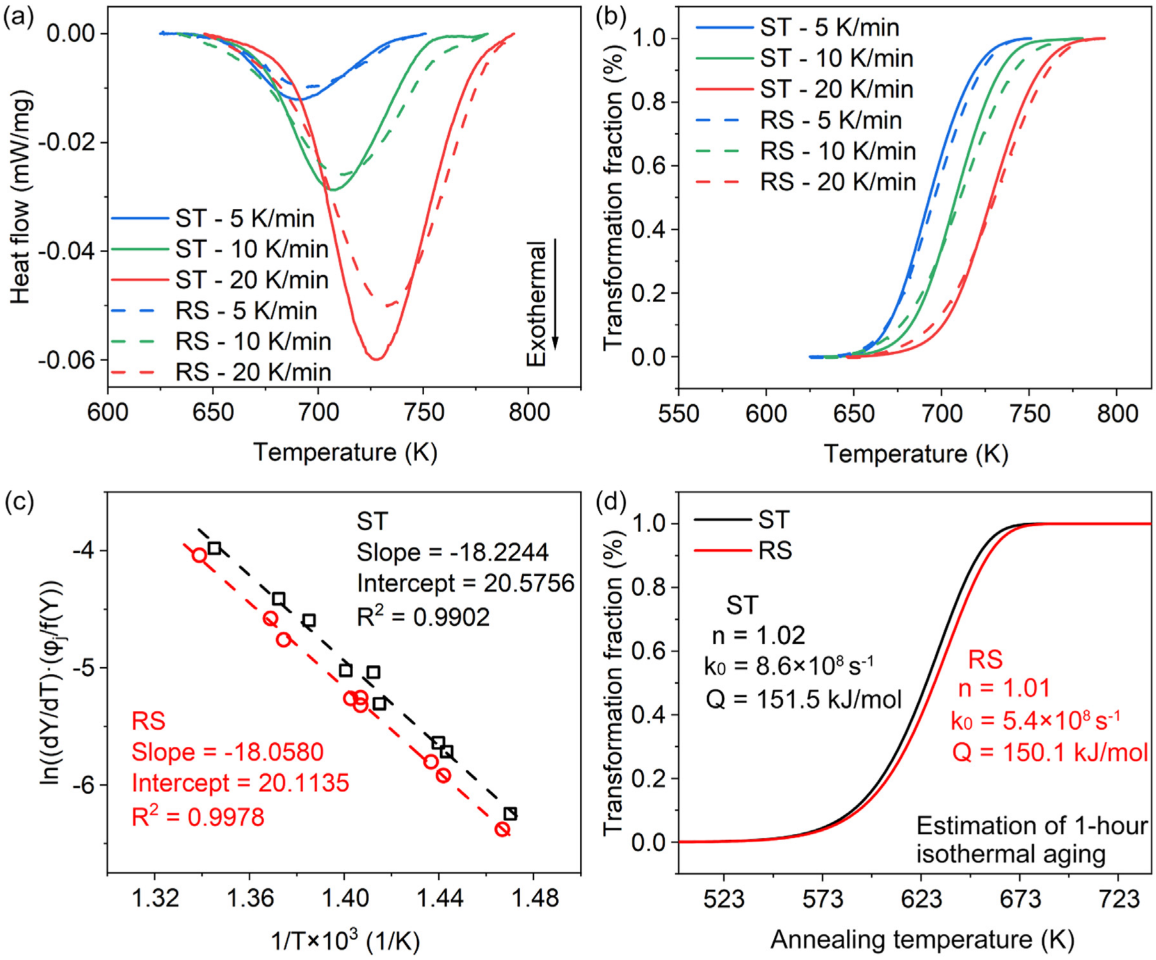

Fig. 14. DSC curves and precipitation kinetics analysis. (a) DSC curves of precipitation reactions of ST and $RS_{3.0}$ samples at different heating rates; (b) the curve of precipitation volume fraction Y relative to temperature at different heating rates; (c) $\ln(\varphi_j \cdot dY/dT)$ for linear fitting of $1/T$. (d) Assuming that the value of n remains constant during the precipitation process, the transformation fractions at different annealing temperatures under isothermal annealing for 1 h.

where A is the entropy factor, E_f is the vacancy formation energy, k_B is the Boltzmann constant, and T is the absolute temperature. Vacancy concentration increases exponentially with temperature. The ST sample, rapidly quenched from a temperature near the melting point, possesses a high vacancy concentration. The solute diffusion in the precipitation process is typically a vacancy-driven process, where, in Cu-Ni-Be alloys, vacancies first facilitate the diffusion of monolayer Be atoms, followed by the enrichment of Ni atoms around the Be atoms to form the γ'' phase [6].

Due to the high vacancy concentrations in both the ST and $RS_{3.0}$ samples, the two alloys exhibit similar Q and n values. With increasing temperature, the $RS_{3.0}$ sample, compared to the ST sample, not only undergoes solute dissolution but also shows dislocation recovery (Fig. 4). Specifically, during dislocation recovery, dislocation movement interacts with vacancies, causing them to be absorbed, which leads to a reduction in vacancy density. Consequently, vacancy mobility and diffusion rates decrease, resulting in a temporary suppression of precipitation in the $RS_{3.0}$ sample. This is reflected in the reduced k_0 value during precipitation kinetics. As the temperature continues to rise, vacancy oscillation intensifies, and the vacancy density increases exponentially with T. This allows the $RS_{3.0}$ sample to achieve a similar volume fraction of the precipitate phase and the same ΔH as the ST sample.

4.2. Strengthening and toughening mechanism

RS deformation refines the grain size and introduces a large number of dislocations, thereby enhancing the material's strength. The primary strengthening mechanisms are dislocation strengthening and GB strengthening. Aging treatment further strengthens the material through the formation of nanoscale precipitates. It is essential to investigate the changes in strength during the aging process for both the ST and $RS_{3.0}$ samples, Fig. 16(a) and (b) shows the difference in yield strength ($\Delta\sigma_{0.2}$) and UTS ($\Delta\sigma_{\mathrm{UTS}}$) respectively, between the aged and original states of the two samples. For the ST sample (black solid squares), a significant increase in both $\Delta\sigma_{0.2}$ and $\Delta\sigma_{\mathrm{UTS}}$ is observed with aging temperature, peaking at approximately 673 K and 723 K in $\Delta\sigma_{0.2}$ and $\Delta\sigma_{\mathrm{UTS}}$, respectively. Beyond this temperature, both metrics sharply decrease, indicating overaging. Conversely, for the $RS_{3.0}$ sample (red open circles), the enhancements in strength are notably reduced compared to the ST sample, especially at higher temperatures. The $\Delta\sigma_{0.2}$ and $\Delta\sigma_{\mathrm{UTS}}$ values for $RS_{3.0}$ show a much smaller peak at around 673 K and decline steeply afterward, even becoming negative at 873 K.

The diminished strengthening in the $RS_{3.0}$ sample is likely attributable to: (I) Dislocation recovery in aging process; (II) The precipitation kinetics was slightly suppressed during aging, resulting

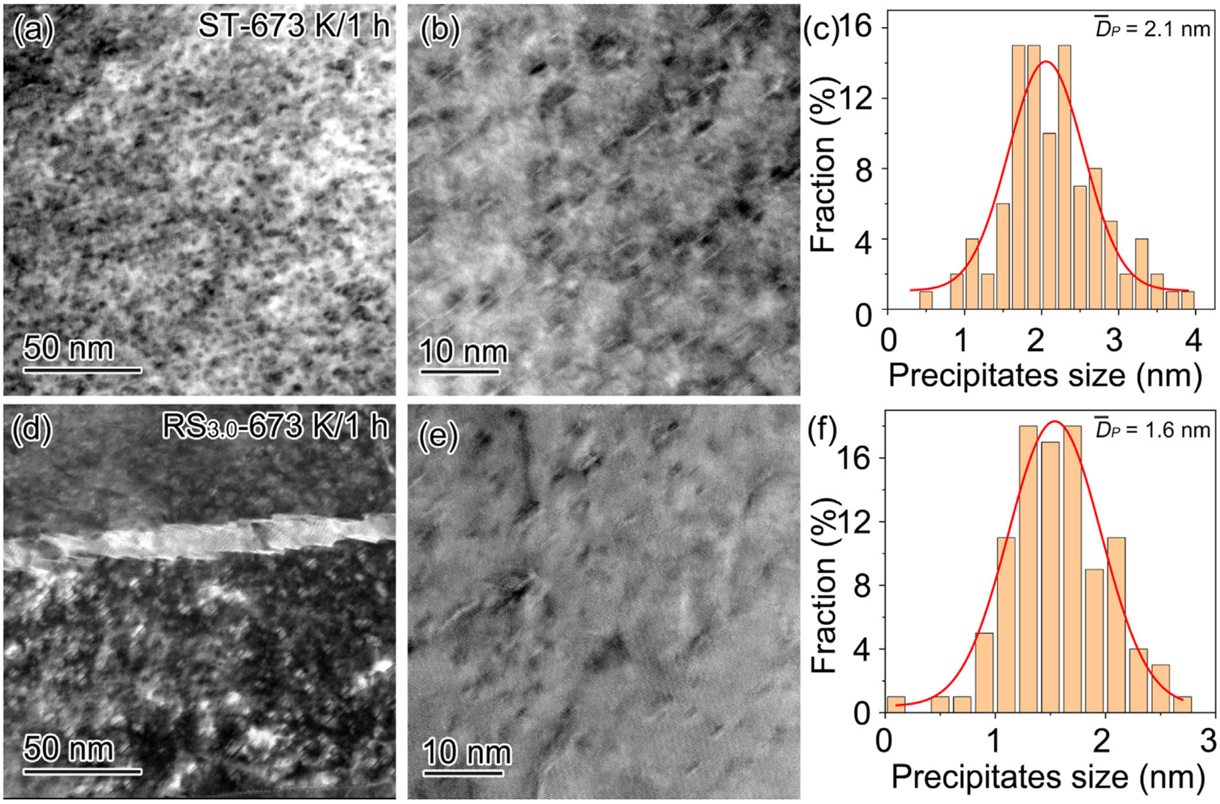

Fig. 15. The distribution of precipitates of aged samples of ST (a–c) and $RS_{3.0}$ (d–f). (a, d) HAADF; (b, e) HRTEM; (c, f) size distribution of precipitates.

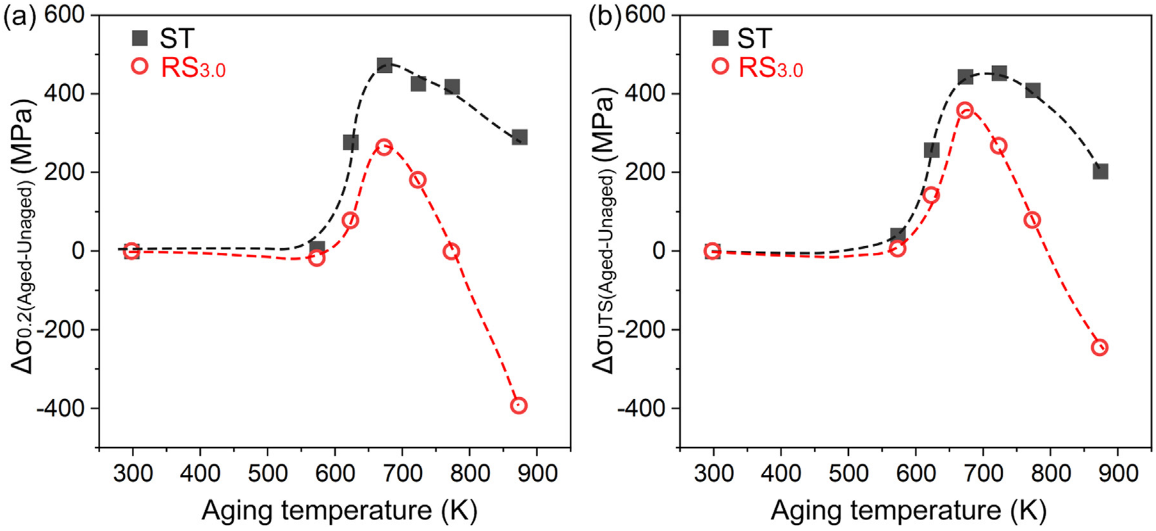

Fig. 16. The strength differences between the aged and original states of two samples ST and $RS_{3.0}$. (a) $\Delta\sigma_{0.2(\text{Aged-Unaged})}$; (b) $\Delta\sigma_{\text{UTS(Aged-Unaged)}}$.

in smaller precipitates than the ST sample. For the former, dislocation strengthening (σ_d) is dependent on the dislocation density and can be estimated using the following equation [38]:

$$\sigma_d = M\alpha 1 G_m b\rho^{1/2} \tag{10}$$

where M is the average Taylor factor, α_1 is constant, G_m is the shear modulus of the matrix, b is the burgers vector, and ρ is the dislocation density. Therefore, the strengthening effect is reduced due to the decrease in dislocation density during aging in the $RS_{3.0}$ sample.

For the latter, nanoscale precipitates with small sizes are more likely to be cut by dislocations during plastic deformation, leading to a strengthening effect. Coherency strengthening (σ_{cs}), modulus mismatch strengthening (σ_{ms}), and ordered strengthening (σ_{os}) are the three fundamental aspects of the shearing mechanism, they can be estimated by the following formula [39]:

$$\sigma_{cs} = M \cdot \alpha_\varepsilon (G \cdot \varepsilon)^{3/2} \left(\frac{rf}{0.5Gb} \right)^{1/2} \tag{11}$$

$$\sigma_{ms} = M \cdot 0.0055 (\Delta G)^{3/2} \left(\frac{2f}{G} \right)^{1/2} \left(\frac{r}{b} \right)^{3m/2-1} \tag{12}$$

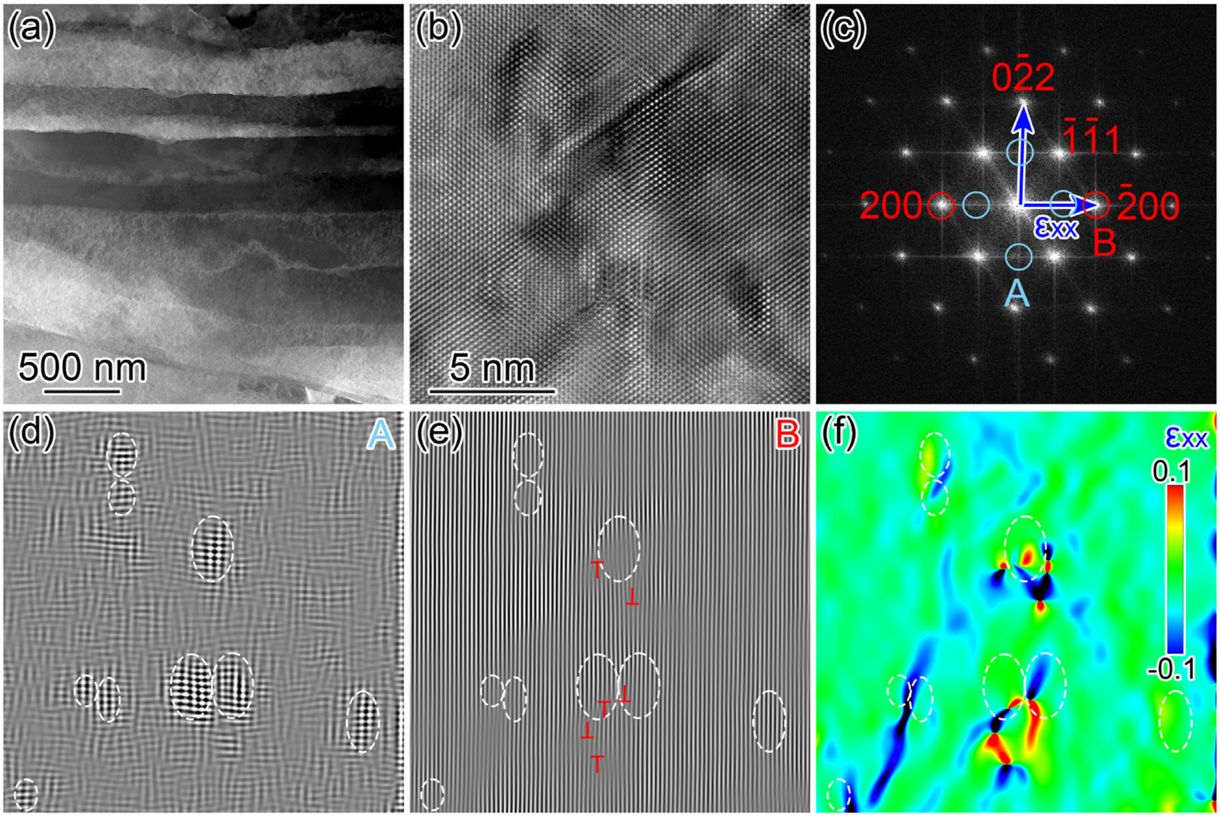

Fig. 17. Microstructure of RS$_{3.0}$–673 K/1 h sample after tensile deformation. (a) Low magnification HAADF image; (b) HRTEM; (c) FFT image of (b); (d) IFFT image based on the blue circle shown in A in (c); (e) IFFT image based on the red circle shown in B in (c); (f) GPA analysis based on ε_{xx} in (c).

$$\sigma_{\mathrm{os}} = M \cdot 0.81 \frac{\gamma_{APB}}{2b} \left(\frac{3\pi f}{8} \right)^{1/2} \tag{13}$$

where $\alpha_{\varepsilon} = 2.6$ in FCC structure, ε approximately $2/3(\Delta a/a)$. Δa is the difference between lattice parameters of matrix and precipitation [40,41], m is a constant, f is the volume fraction of the precipitates, ΔG is the difference between the shear modulus of matrix and precipitation, and γ_{APB} is the antiphase boundary energy. Therefore, the precipitation strengthening effect of the RS$_{3.0}$–673 K/1 h sample is lower than that of the ST-673 K/1 h sample, despite the precipitation phase density being similar between the two alloys and the size of the RS$_{3.0}$–673 K/1 h alloy being smaller. It is worth noting that, in general, the strengthening observed during aging in samples prepared via the deformation plus aging process is often less significant than that achieved through direct aging of the solution-treated state [5]. However, some anomalous phenomena exist. For instance, in NC alloys, when there is GB segregation [42] or precipitates pinning the GBs [43], the strengthening effect achieved by aging can exceed that of coarse-grained alloys by more than twice.

To investigate the strengthening and toughening mechanisms during tensile deformation, TEM analysis was conducted on the gauge section of the post-testing tensile specimens, as shown in Fig. 17The microstructure reveals fibrous grains with a high density of dislocations (Fig. 17(a)), without evidence of twinning or phase transformation induced by the tensile process. HRTEM imaging shows that precipitates are challenging to identify directly due to the influence of the dislocation stress field (Fig. 17(b)). To resolve this, FFT was applied to Fig. 17(b), and the characteristic FFT spots for the γ'' phase (circled in blue in Fig. 17(c)) were selected for IFFT transformation. The resulting image (Fig. 17(d)) reveals a high-density distribution of precipitates.

Additionally, selecting the (200) spot in Fig. 17(c) (circled in red) for IFFT reveals the presence of dislocations both near and within the precipitates, as indicated by the "⊥" symbols in Fig. 17(e). GPA analysis further indicates significant strain in the vicinity of dislocations, while lattice distortion is also present around and within the precipitates in dislocation-free regions, as shown in Fig. 17(f). Precipitates can enhance the work-hardening capacity of a material by impeding dislocation movement during deformation. This interaction increases the resistance to dislocation motion, requiring higher applied stresses for further plastic deformation. The result is an accumulation of dislocations around the precipitates, creating internal stress fields that strengthen the material. Additionally, as more dislocations accumulate, the likelihood of dislocation interactions and entanglements rises, further contributing to work-hardening. This mechanism effectively enhances both the strength and work-hardening rate of the material.

4.3. Conductivity optimization mechanism

According to Matthiessen's rule [44], the resistivity of an alloy is influenced by its microstructure, including GBs, dislocations, phase interface, precipitates, etc. The resistivity can be expressed as:

$$\Omega = \Omega_{\mathrm{Cu}} + \Omega_{\mathrm{GB}} + \Omega_{\mathrm{S}} + \Omega_{\mathrm{Dis}} + \Omega_{\mathrm{P}} \tag{14}$$

where Ω_{Cu} is the resistivity of pure copper (1.724×10^{-8} Ω m), Ω_{GB} and Ω_{Dis} are the resistivities due to GBs and dislocations, respectively, Ω_{P} is the resistivity from precipitates, and Ω_{S} is the resistivity contribution from solute atoms. Factors such as precipitate size and distribution, grain size and shape, dislocation density, and lattice distortions each impact electrical conductivity to varying degrees.

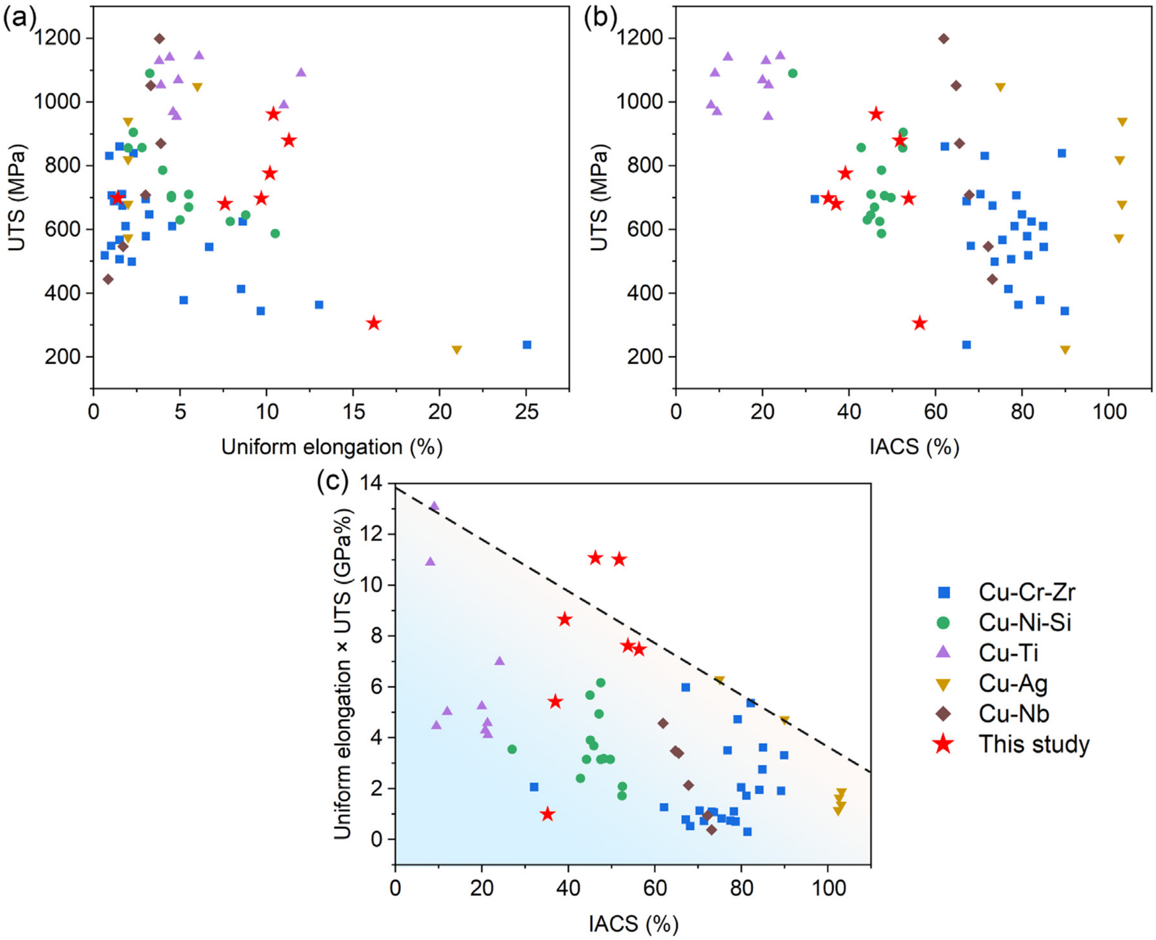

Fig. 18. Comprehensive tensile performance of Cu-Cr-Zr [47–58], Cu-Ni-Si [59–64], Cu-Ag [65,66], Cu-Nb [67] based alloys and composite materials in the literature are compared with RS Cu-Ni-Be. (a) UTS versus uniform elongation; (b) UTS versus electrical conductivity; (c) product of uniform elongation and UTS versus electrical conductivity.

In coarse-grained pure copper, HAGBs are the primary lattice defects affecting conductivity. The low density of GBs in coarse-grained copper results in a high electrical conductivity (100 % IACS). In contrast, for alloys, the effect of different solute elements on electrical conductivity varies significantly. For solute contents <0.1 wt.%, the impact on conductivity, from most to least detrimental, is as follows: Ti, Fe, Co, Be, Ni, and Ag [45]. Additionally, in Cu-Ni-Be alloys, the solubility of Be in the copper matrix at room temperature is very low, and Be tends to combine with Ni after aging [46]. Consequently, the precipitation during aging reduces the concentrations of Be and Ni solute atoms in the matrix, leading to a significant enhancement in electrical conductivity. On the other hand, the introduction of high-density dislocations through RS hurts conductivity. However, compared to the 24 µm grain size of the ST sample, RS increases the grain length along the wire axis to 106 µm, which significantly reduces the effect of HAGBs on conductivity. Therefore, the electrical conductivity of the alloy produced by RS and aging is essentially the result of a competition between GB density, dislocation density, and solute atom content, and GB density is dominant. In comparison to other deformation methods that produce equiaxed ultrafine-grained alloys, the RS process offers a distinct advantage in optimizing electrical conductivity.

For conductive materials with excellent performance, it is essential to achieve a balance between high strength, ductility, and electrical conductivity. A comparison of literature data reveals an inverse relationship between strength and ductility in different copper alloys and copper-based composites. In this study, the Cu-Ni-Be alloy produced by RS and subsequent aging demonstrates an outstanding combination of UTS and uniform elongation. It is worth noting that the Cu-Ti alloy, which breaks this inverse relationship, shows even greater advantages in this regard (Fig. 18(a)). On the other hand, Cu-Ti alloys exhibit significantly lower electrical conductivity, not exceeding 25 % IACS (Fig. 18(b)). When considering mechanical properties through a combination of uniform elongation and tensile strength, and examining their relationship with electrical conductivity, the Cu-Ni-Be alloy fabricated by RS shows superior overall mechanical and electrical performance, breaking the traditional inverse relationship, as shown in Fig. 18(c). These characteristics highlight the potential of RS Cu-Ni-Be alloys for industrial applications.

5. Conclusions

This paper focused on Cu-Ni-Be alloys, utilizing RS deformation to process coarse-grained Cu-Ni-Be rods, followed by aging to enhance material properties. The result is high-strength, high-toughness, and high-conductivity Cu-Ni-Be alloy wires. Although Cu-Ni-Be alloys, with their high stacking fault energy, cannot achieve nanoscale grains, the dispersed nanoscale precipitates provide both strength and work-hardening capacity. The main findings are summarized as follows:

(1) Following multiple passes of RS, the performance differences between the core and edge regions of the RS Cu-Ni-Be alloy are minimal, near homogeneous structures. The core of the Cu-Ni-Be alloy achieved a tensile strength of 706 MPa,

uniform elongation of 1.4 %, and electrical conductivity of 35 % IACS. After aging at 673 K for 1 h, these values increased to a tensile strength of 1064 MPa, uniform elongation of 10.4 %, and conductivity of 46 % IACS.

(2) The core region of the RS Cu-Ni-Be alloy exhibited fibrous grains with a width of 0.92 μm and a length of 106 μm, featuring a strong $\langle 111\rangle$ and a relatively weaker $\langle 001\rangle$ fiber texture along the wire axis. After aging at 673 K/1 h, the dislocation density slightly decreased, with nanoscale γ'' precipitates dispersed throughout the structure, while the texture remained largely unchanged. Aging at higher temperatures led to recrystallization, reducing the strength and displaying a texture inheritance effect.

(3) There is no apparent dependence of GBs and dislocations on the aging process of RS Cu-Ni-Be alloys. Compared to direct aging of the ST sample, RS deformation slightly inhibits precipitation kinetics, which may be related to the vacancy density in the sample.

(4) TEM analysis of the tensile-tested samples revealed dislocations near and within the γ'' precipitates, indicating that these precipitates act as barriers to dislocation motion, thus enhancing the strength and work-hardening capacity of the alloy. The elongated grains along the wire axis reduce the contribution of HAGBs to resistivity, helping to break the traditional strength-conductivity trade-off.

(5) The combination of RS and aging treatment makes the produced Cu-Ni-Be alloy have excellent overall properties and are suitable for industrial applications.

Declaration of competing interest

The authors declare that they have no known competing financial interests or personal relationships that could have appeared to influence the work reported in this paper.

CRediT authorship contribution statement

Kaixuan Zhou: Writing – review & editing, Writing – original draft, Visualization, Methodology, Investigation, Formal analysis, Data curation. **Yonghao Zhao:** Writing – review & editing, Supervision, Resources, Project administration, Investigation, Funding acquisition, Formal analysis, Data curation, Conceptualization. **Qingzhong Mao:** Project administration, Investigation, Funding acquisition. **Shunqiang Li:** Methodology. **Jizi Liu:** Writing – review & editing, Supervision, Resources, Project administration, Methodology, Investigation, Funding acquisition, Formal analysis, Conceptualization.

Acknowledgements

The authors would like to acknowledge financial support from the National Key R&D Program of China (Grant No 2021YFA1200203), the National Natural Science Foundation of China (Grant Nos. 51971112, 51225102, and 52171119), the Jiangsu Province Leading Edge Technology Basic Research Major Project (BK20222014), the Fundamental Research Funds for the Central Universities (No. 2023201001), the Jiangsu Funding Program for Excellent Postdoctoral Talent (Grant No 2023ZB091), and the China Postdoctoral Science Foundation (Grant No 2023M741699). The authors also want to acknowledge the support of the Jiangsu Key Laboratory of Advanced Micro-Nano Materials and Technology. SEM, TEM, and EBSD experiments are performed at the Center of Analytical Facilities of Nanjing University of Science and Technology. Thanks eceshi (www.eceshi.com) for providing the direct-reading spectrometer used for component detection.

References

[1] K. Yang, Y. Wang, M. Guo, H. Wang, Y. Mo, X. Dong, H. Lou, Prog. Mater. Sci. 138 (2023) 101141.
[2] Y. Zhou, Y. Liu, K. Song, S. Li, C. Feng, Q. Zhu, X. Peng, S. Yang, X. Li, P. Zhang, Mater. Today Commun. 33 (2022) 104819.
[3] H. Yang, Z. Ma, C. Lei, L. Meng, Y. Fang, J. Liu, H. Wang, Sci. China Technol. Sci. 63 (2020) 2505–2517.
[4] J.R. Davis, Copper and Copper Alloys, ASM International, Materials Park, 2001.
[5] I. Lomakin, M. Castillo-Rodríguez, X. Sauvage, Mater. Sci. Eng. A 744 (2019) 206–214.
[6] B. Zhang, J. Wang, Y. Meng, Z. Hong, H. Zhao, X. Dong, Mater. Des. 238 (2024) 112666.
[7] Y.H. Xu, H.L. Zhao, Y.H. Fan, Z.Y. Hong, K.X. Song, X.L. Dong, C.W. Guo, J. Alloy. Compd. 909 (2022) 164680.
[8] C. Elibol, Mater. Today Commun. 31 (2022) 103473.
[9] A. Mohammadi, X. Sauvage, F. Cuvilly, K. Edalati, J. Mater. Sci. Technol. 203 (2024) 269–281.
[10] S. Fan, Z. Li, W. Xiao, P. Yan, J. Feng, Q. Jiang, J. Ma, Y. Gong, J. Mater. Sci. Technol. 188 (2024) 202–215.
[11] Q.Z. Mao, Y.S. Zhang, Y.Z. Guo, Y.H. Zhao, Commun. Mater. 2 (2021) 1–9.
[12] Q.Z. Mao, Y.S. Zhang, J.Z. Liu, Y.H. Zhao, Nano Lett. 21 (2021) 3191–3197.
[13] Q.Z. Mao, L. Wang, J.F. Nie, Y.H. Zhao, Compos. Part B-Eng. 231 (2022) 109567.
[14] K. Zhou, Y. Zhao, Q. Mao, B. Zhu, G. Sun, S. Li, J. Liu, J. Mater. Process. Technol. 330 (2024) 118489.
[15] Y.C. Wan, B. Tang, Y.H. Gao, L.L. Tang, G. Sha, B. Zhang, N.N. Liang, C.M. Liu, S.N. Jiang, Z.Y. Chen, X.Y. Guo, Y.H. Zhao, Acta Mater. 200 (2020) 274–286.
[16] Y. Yang, X. Chen, J.F. Nie, K. Wei, Q.Z. Mao, F.H. Lu, Y.H. Zhao, Mater. Res. Lett. 9 (2021) 255–262.
[17] X. Chen, C.M. Liu, Y.C. Wan, S.N. Jiang, Z.Y. Chen, Y.H. Zhao, Metall. Mater. Trans. A 52 (2021) 4053–4065.
[18] Y. Yang, J.F. Nie, Q.Z. Mao, Y.H. Zhao, Res. Phys. 13 (2019) 102236.
[19] F.H. Lu, J.F. Nie, X. Ma, Y.S. Li, Z.W. Jiang, Y. Zhang, Y.H. Zhao, X.F. Liu, Mater. Sci. Eng. A 770 (2020) 138519.
[20] J.F. Nie, F.H. Lu, Z.W. Huang, X. Ma, H. Zhou, C. Chen, X. Chen, H.B. Yang, Y. Cao, X.F. Liu, Y.H. Zhao, Y.T. Zhu, Materialia 9 (2020) 100523.
[21] A. Meng, X. Chen, J.F. Nie, L. Gu, Q.Z. Mao, Y.H. Zhao, J. Alloy. Compd. 859 (2021) 158222.
[22] Q.Z. Mao, X. Chen, J.S. Li, Y.H. Zhao, Nanomaterials 11 (2021) 2223.
[23] Q.Z. Mao, Y.F. Liu, Y.H. Zhao, J. Alloy. Compd. 896 (2022) 163122.
[24] K. Zhou, Y. Zhao, H. Dong, Q. Mao, S. Jin, M. Feng, R. Zhang, S. Li, J. Liu, Nano Today 56 (2024) 102234.
[25] J.B. Nelson, D.P. Riley, Proc. Phys. Soc. 57 (1945) 160.
[26] R. Monzen, C. Watanabe, T. Seo, T. Sakai, Phil. Mag. Lett. 85 (2005) 603–612.
[27] Z.Y. Zhu, Y.F. Cai, Y. Sui, K.X. Song, Y.J. Zhou, J.S. Zou, Materials 11 (2018) 1394.
[28] L. Yagmur, O. Duygulu, B. Aydemir, Mater. Sci. Eng. A 528 (2011) 4147–4151.
[29] R. Monzen, T. Seo, T. Sakai, C. Watanabe, Mater. Trans. 47 (2006) 2925–2934.
[30] K. Zhou, Y. Zhao, Q. Mao, R. Zhang, S. Li, G. Sun, H. Dong, L. Gu, J. Liu, Compos. Part B-Eng. 276 (2024) 111371.
[31] K.S. Ghosh, A.K. Kumar, M.K. Mohan, Trans. Ind. Instit. Metals 61 (2008) 487–496.
[32] A. Luo, D.J. Lloyd, A. Gupta, W.V. Youdelis, Acta Metall. Mater. 41 (1993) 769–776.
[33] Y.H. Zhao, X.Z. Liao, Z. Jin, R.Z. Valiev, Y.T. Zhu, Acta Mater. 52 (2004) 4589–4599.
[34] N. Tsuji, T. Iwata, M. Sato, S. Fujimoto, Y. Minamino, Sci. Technol. Adv. Mater. 5 (2016) 173–180.
[35] E.A. Prokofiev, J.A. Burow, E.J. Payton, R. Zarnetta, J. Frenzel, D.V. Gunderov, R.Z. Valiev, G. Eggeler, Adv. Eng. Mater. 12 (2010) 747–753.
[36] X. Sauvage, N. Enikeev, R. Valiev, Y. Nasedkina, M. Murashkin, Acta Mater. 72 (2014) 125–136.
[37] G. Thomas, J. Washburn, Rev. Mod. Phys. 35 (1963) 992.
[38] E. Nes, T. Pettersen, K. Marthinsen, Scr. Mater. 43 (2000) 55–62.
[39] J.Y. He, H. Wang, H.L. Huang, X.D. Xu, M.W. Chen, Y. Wu, X.J. Liu, T.G. Nieh, K. An, Z.P. Lu, Acta Mater. 102 (2016) 187–196.
[40] W.B. Pearson, A Handbook of Lattice Spacings and Structures of Metals and Alloys, Pergamon Press, Oxford, 1964.
[41] D. Liu, B. Huang, C. Wang, J. Ma, X. Zhao, J. Mater. Eng. Perform. 31 (2022) 9910–9920.
[42] R. Yang, Z. Feng, T. Huang, G. Wu, A. Godfrey, X. Huang, Scr. Mater. 206 (2022) 114240.
[43] X.L. Liang, D.Y. Liu, Z.L. Shen, N.R. Tao, Scr. Mater. 247 (2024) 116118.
[44] A. Matthiessen, A.C.C. Vogt, Philos. Trans. R. Soc. London 154 (1864) 167–200.
[45] S.Z. Han, E.-A. Choi, S.H. Lim, S. Kim, J. Lee, Prog. Mater. Sci. 117 (2021) 100720.
[46] A. Takeuchi, A. Inoue, Mater. Trans. 46 (2005) 2817–2829.
[47] G.Y. Li, S.Y. Li, L. Li, D.T. Zhang, J.D. Wang, Y.X. Tong, Vacuum 190 (2021) 110315.
[48] Y.X. Tong, Y. Wang, Z.M. Qian, D.T. Zhang, L. Li, Y.F. Zheng, Acta Metall. Sin.-Engl. Lett. 31 (2018) 1084–1088.
[49] R. Li, E. Guo, Z. Chen, H. Kang, W. Wang, C. Zou, T. Li, T. Wang, J. Alloy. Compd. 771 (2019) 1044–1051.
[50] S. Zhang, R. Li, H. Kang, Z. Chen, W. Wang, C. Zou, T. Li, T. Wang, Mater. Sci. Eng. A 680 (2017) 108–114.
[51] A. Meng, J. Nie, K. Wei, H. Kang, Z. Liu, Y. Zhao, Vacuum 167 (2019) 329–335.
[52] L.X. Sun, N.R. Tao, K. Lu, Scr. Mater. 99 (2015) 73–76.

[53] R. Mishnev, I. Shakhova, A. Belyakov, R. Kaibyshev, Mater. Sci. Eng. A 629 (2015) 29–40.
[54] Z.Y. Zhang, L.X. Sun, N.R. Tao, J. Mater. Sci. Technol. 48 (2020) 18–22.
[55] N. Liang, J. Liu, S. Lin, Y. Wang, J.T. Wang, Y. Zhao, Y. Zhu, J. Alloy. Compd. 735 (2018) 1389–1394.
[56] A.H. Huang, Y.F. Wang, M.S. Wang, L.Y. Song, Y.S. Li, L. Gao, C.X. Huang, Y.T. Zhu, Mater. Sci. Eng. A 746 (2019) 211–216.
[57] Y. Wang, R. Fu, Y. Li, L. Zhao, Mater. Sci. Eng. A 755 (2019) 166–169.
[58] G. Purcek, H. Yanar, D.V. Shangina, M. Demirtas, N.R. Bochvar, S.V. Dobatkin, J. Alloy. Compd. 742 (2018) 325–333.
[59] W. Wang, H. Kang, Z. Chen, Z. Chen, C. Zou, R. Li, G. Yin, T. Wang, Mater. Sci. Eng. A 673 (2016) 378–390.
[60] C. Watanabe, S. Takeshita, R. Monzen, Metall. Mater. Trans. A 46 (2015) 2469–2475.
[61] Q. Lei, Z. Li, T. Xiao, Y. Pang, Z.Q. Xiang, W.T. Qiu, Z. Xiao, Intermetallics 42 (2013) 77–84.
[62] Y. Ban, Y. Geng, J. Hou, Y. Zhang, M. Zhou, Y. Jia, B. Tian, Y. Liu, X. Li, A.A. Volinsky, J. Mater. Sci. Technol. 93 (2021) 1–6.
[63] S. Chenna Krishna, J. Srinath, A.K. Jha, B. Pant, S.C. Sharma, K.M. George, J. Mater. Eng. Perform. 22 (2013) 2115–2120.
[64] C. Wang, H. Fu, H. Zhang, X. He, J. Xie, Mater. Sci. Eng. A 838 (2022) 142815.
[65] C. You, W. Xie, S. Miao, T. Liang, L. Zeng, X. Zhang, H. Wang, Mater. Des. 200 (2021) 109455.
[66] X. Zhu, Z. Xiao, J. An, H. Jiang, Y. Jiang, Z. Li, J. Alloy. Compd. 883 (2021) 160769.
[67] C. Ding, J. Xu, D. Shan, B. Guo, T.G. Langdon, Compos. Part B-Eng. 211 (2021) 108662.